

Finite-temperature Coulomb Excitations in Extrinsic Dirac Structures

Andrii Iurov*

*Center for High Technology Materials, University of New Mexico,
1313 Goddard SE, Albuquerque, NM, 87106, USA*

Godfrey Gumbs

*Department of Physics and Astronomy, Hunter College of the City University of New York,
695 Park Avenue, New York, NY 10065, USA and
Donostia International Physics Center (DIPC), P de Manuel Lardizabal,
4, 20018 San Sebastian, Basque Country, Spain*

Danhong Huang

*Air Force Research Laboratory, Space Vehicles Directorate,
Kirtland Air Force Base, NM 87117, USA and
Center for High Technology Materials, University of New Mexico,
1313 Goddard SE, Albuquerque, NM, 87106, USA*

Ganesh Balakrishnan

*Center for High Technology Materials, University of New Mexico,
1313 Goddard se, Albuquerque, NM, 87106, USA*

(Dated: July 28, 2017)

We have derived algebraic, analytic expressions for the chemical potential without any restriction on temperature for all types of doped, or extrinsic, gapped Dirac cone materials including gapped graphene, silicene, germanene and single-layer transition metal dichalcogenides. As an important intermediate step of our derivations, we have established a reliable piecewise-linear model for calculating the density-of-states in molybdenum disulfide, showing good agreement with previously obtained numerical results. For the spin- and valley-resolved band structure, we obtain an additional decrease of the chemical potential due to thermally induced doping of the upper subband at finite temperature. It has been demonstrated that since the symmetry between the electron and hole states in MoS_2 is broken, the chemical potential could cross the zero-energy level at sufficiently high temperature. These results allow us to investigate the collective properties, polarizability, plasmons and their damping. Emphasis is placed on low temperatures, when initial electron doping plays a crucial role. We clearly demonstrated the contribution of the initial doping to the finite-temperature collective properties of the considered materials.

PACS numbers: 73.21.-b, 73.63.-b, 71.45.Gm, 73.20.Mf

I. INTRODUCTION

Despite the fact that the microscopic properties of various low-dimensional materials have been meticulously examined over a fairly long period of time, ^{1,2} only successful fabrication of graphene in 2004 ^{3,4} stimulated an intriguingly new research effort devoted to the study of atomically thin two-dimensional (2D) materials. In particular, it was by virtue of its unique, yet unexpected massless Dirac electronic properties that led to high mobility (200,000 cm²/V-s) and ballistic transport properties. ⁵⁻⁷ In the corners of the Brillouin zone, referred to as K and K' points, there is no energy band gap and the dispersions represent a linear Dirac cone structure. Due to the existence of such an energy spectrum, opening a sufficiently large and tunable energy gap in graphene has become an important issue in order to enable electron confinement. Researchers tried to achieve this by adjoining a variety of insulating substrates ⁸⁻¹¹ or even exfoliated graphene to circularly-polarized radiation. ¹² In finite-width nanoribbons, their energy band structure and gap are modified by the type of insulating ‘cousin’ that is introduced. ¹³⁻¹⁵

In order to create a truly tunable band gap, one must use a material with large spin-orbit coupling or a buckled structure. In this regard, silicene, a 2D silicon structure was deemed a good candidate. Single-monolayer Si possesses a buckled structure simply because of the larger ionic size of silicon compared to carbon. This results in a large spin-orbit band gap 1.55 meV and the possibility to modify its energy spectrum by applying an external perpendicular electric field ¹⁶⁻¹⁸. These properties make it display an experimentally realizable KaneMele type of quantum spin Hall effect, or a topological insulator state, because of the existence of time-reversal symmetry. ^{19,20} Unlike graphene, the band structure of silicene and its nanoribbons ²¹⁻²³ directly depends on spin and valley indices which give lead to plenty of nanoelectronic, valleytronic and spintronic applications.

Germanene, the most recently discovered and fabricated member of atomically thin buckled 2D honeycomb lattices,^{24–29} demonstrates substantially larger Fermi velocities and a band gap of $20 - 90\text{ meV}$. Grown by molecular beam epitaxy³⁰ and investigated with x-ray absorption spectroscopy, *Ge* layers demonstrated satisfactory agreement between the experimentally obtained and theoretically predicted results for its inter-atomic distance.

Another important class of innovative 2D materials is represented by direct-gap transition metal dichalcogenides, or TMDC's. Its chemical makeup consists of a transition metal atom *M*, such as molybdenum or tungsten, and two identical chalcogens *C*, i.e., sulfur, selenium or tellurium. Schematically, TMDC's are described as MC_2 . In our consideration, we are mostly going to focus on *MoS*₂, as their most studied representative. This material exhibits a semiconductor energy band structure with a very large direct gap 1.78 eV , in contrast to its bulk states with indirect gap 1.3 eV , and substantial spin-orbit coupling.³¹ Strictly speaking, *MoS*₂ is not a Dirac material since the mass terms play a crucial role in its energy dispersions, however its low-energy Hamiltonian contains a $t_0 a_0 \Sigma \cdot \mathbf{k}$ term, corresponding to the linear Dirac cone dispersion.

An effective two-band continuum model and lattice Hamiltonian,³² based on the tight-binding model, accounts for the hybridization of the *d* orbitals in *Mo* and the *p* orbitals of sulfur atoms. It gives an adequate description of its low-energy band structure and predicts large spin splitting.³³ Due to the breaking of inversion symmetry and spin-orbit coupling, spin and valley physics is observed in all group-IV dichalcogenides, including *MoS*₂.³⁴ The low-energy states of such systems are no longer massive Dirac fermions since there is a difference between electron and hole masses as well as trigonal warping effects.³⁵ Strain engineering, used to tune optical and electronic properties of conventional semiconductors, has also been applied to molybdenum disulfide, and its modified band structure has been theoretically calculated.³⁶ These unique electronic properties of a single-layer *MoS*₂ were later used to create high-performance transistors operating at room temperature.³⁷ These electronic models and effective Hamiltonian have been widely used to investigate the collective properties of TMDC's³⁸ and their influence on the gap transition.³⁹ In optoelectronics, the band structure, spin and valley properties of molybdenum disulfide could be successfully controlled by off-resonant dressing field.⁴⁰

Current many-body and quantum field theory methods in condensed matter physics^{41,42} have provided helpful ways to understand the electronic and transport properties of low-dimensional solids, including diverse bucked honeycomb materials.^{43–45} In most of these theories, we find the *dynamical polarization function*, or polarizability, to be the mainstay, fundamental quantity, describing the screening of an external potential by interacting electrons.^{38,46–49} Also, the dynamic polarization function plays a key role in calculating the plasmon excitations, due to the charge density oscillations, which occur in metals and semiconductors. Specifically, the plasmon dispersion relation along with their lifetimes have been theoretically investigated for a wide range of 2D Dirac systems.^{47,50–55} The interest in graphene plasmons is due in part to the fact that these excitations have no classical counterpart.⁵⁶ There has also been a considerable experimental effort for investigating graphene plasmons, gate-tuning, infrared nano-imaging and confinement^{57–61} Graphene plasmonic resonances and instability at various wavelengths could be used in photodetectors in the Terahertz range.⁶² All these techniques could be successfully applied to the recently fabricated materials, discussed in the present work.

Plasmonic applications have been widely based on *nanoscale hybrid systems*, in which graphene plasmons are coupled to a surface plasmon excitations in metals. Technology has now gone a long way in combining graphene with prefabricated plasmonic nanoarrays and metamaterials in order to produce plasmonics-based tunable hybrid optical devices.⁶³ Therefore, accurate knowledge of plasmon mode dispersions in graphene interfaced with metallic substrates is crucial. Graphene-metal contacts are important components for all such devices. Consequently, exploration of plasmon modes at these metallic interfaces is a mandatory step toward fabricating the devices. High-resolution electron energy loss spectroscopy (EELS) has been employed to investigate those excitations at the surface of *Bi*₂*Se*₃ to disclose the interplay between surface and Dirac plasmons in topological insulators⁶⁴. Plasmons, their behavior, dispersions, quenching and environmental effects have been thoroughly studied in epitaxial graphene, in air-exposed graphene-*Ru* contacts, Graphene on *Pt*₃*Ni* (111), graphene grown on *Cu* (111) foils.^{65–69}

In all cases under consideration, we need to distinguish between *extrinsic*, or a sample initially doped at $T = 0$, and intrinsic materials, with zero Fermi energy and completely empty conduction band. In the latter case, both the plasmon excitations and the electrical conductivity are completely suppressed at zero temperature due to the absence of free charge carriers. However, at finite temperature, the conduction band would receive thermally induced doping in both cases.^{70,71} In graphene, with zero energy band gap, this density is enhanced as $n \simeq T^2$ and the plasmon dispersion behaves like $\Omega_p^2 \simeq qT$.

The properties of intrinsic finite-temperature plasmon excitations have been systematically examined for various materials including silicene.⁷² In contrast, extrinsic or doped structure at finite temperature is associated with a difficulty to obtain a reliable and accurate value for temperature-dependent chemical potential $\mu(T)$. Generally, it is

known that $\mu(T)$ is decreased as the temperature is increased, and its value could be found based on carrier density conservation^{70,73} In this work, our main objective is to obtain a set of non-integral, transcendental equations for a wide class of Dirac gapped materials with linear density-of-states (DOS), i.e., gapped graphene, silicene, germanene and transition metal dichalcogenides at arbitrary temperature.

However, the range of our considered temperatures is limited by validity of linear or gapped Dirac cone approximation for the energies, which receive noticeable doping at those temperatures. Certain deviations start to build up at about 0.5 eV ,^{74,75} leading to various effect on the plasmons, such as anisotropy, splitting and existence of additional acoustic plasmon branch.^{76,77} Such energies are extremely far away from our range $k_B T \sim E_F^{(0)}$. In all our calculations, the energy is measured in the units of a typical Fermi energy $E_F^{(0)} = 5.22\text{ meV}$, corresponding to electron density $n^{(0)} = 1.0 \cdot 10^{15}\text{ m}^{-2}$.

Once the chemical potential is known, one can obtain the finite-temperature dynamical polarization function by Eq. (18), which is a key component for all relevant many-body calculations. These include optical absorption, electronic transport, plasmon excitations as well as electron exchange and correlation energies.⁷⁸ Here, we pay close attention to finite-temperature plasmons, demonstrating how much initial doping contributes to each branch location at intermediate temperatures. Once the temperature becomes very high, $k_B T \gg E_F$, thermally-induced doping dominates and the contribution from the initial Fermi energy fades away.

The rest of the paper is organized as follows. First, we derive the implicit analytic equations for the finite-temperature chemical potential for all types of Dirac structures with linear DOS in Sec. II. In Sec. III, we calculate the dynamic polarization function which includes the single particle excitation mode frequencies. The single-particle modes combine with a charge cloud to produce weakly interacting quasiparticles that vibrate collectively at the characteristic plasma frequencies. Emphasis has been placed on rather simple cases of gapped graphene and silicene at small, but finite temperatures, when the zero temperature carrier doping plays a crucial role. We also briefly examine *non-local, hybrid* plasmons in an open system of a semi-infinite conductor, Coulomb-coupled to a 2D layer in the presence of finite doping of the electrons in the layer. Our concluding remarks and a concise discussion are presented in Sec. IV. We also provide two appendices with detailed derivations of the DOS for silicene and MoS_2 - in Appendix A, and of the temperature-dependent chemical potential in Appendix B.

II. CHEMICAL POTENTIAL

In this section, we discuss our analytical derivations for the electron chemical potential as a function of temperature. Being equivalent to the Fermi energy at $T = 0$, the chemical potential normally decreases with increasing temperature. Its specific value depends on multiple material parameters such as energy band gaps, Fermi velocities and the DOS of the electrons as well as the holes below the zero energy level. Thus, for a conventional 2D electron gas (2DEG) with no holes, the chemical potential could become negative at a certain temperature, which is not possible for a Dirac system with symmetry between the electron and hole states. Here, we are going to provide closed-form transcendental equations for the finite-temperature $\mu(T)$ for a number of Dirac systems: graphene, buckled honeycomb lattices and transition metal dichalcogenides.

A. Buckled honeycomb lattices

One of the most outstanding features of silicene and other buckled honeycomb lattices is the existence of two generally double degenerate pairs of energy subbands and two inequivalent band gaps. There is a fixed intrinsic spin-orbit gap $2\Delta_{SO}$ and a tunable sublattice-asymmetry gap Δ_z which is induced by and proportional to an applied perpendicular electric field \mathcal{E}_z . For small fields, $\Delta_z = \mathcal{E}_z d_\perp$, where d_\perp is the out-of-plane displacement of a buckled lattice.

The low-energy model Hamiltonian of a buckled honeycomb lattice has been found to be^{16,17}

$$\hat{\mathbb{H}}_{\xi,\sigma} = \hbar v_F (\xi k_x \hat{\tau}_x + k_y \hat{\tau}_y) \otimes \hat{\mathbb{I}}_{2 \times 2} - \xi \Delta_{SO} \hat{\Sigma}_z \otimes \hat{\tau}_z + \Delta_z \hat{\tau}_z \otimes \hat{\mathbb{I}}_{2 \times 2}, \quad (1)$$

where the Fermi velocity $v_F = 0.5 \cdot 10^6\text{ m/s}$ is half that for graphene, $\xi = \pm 1$ is the K/K' valley index, $\tau_{x,y,z}$ and $\Sigma_{x,y,z}$ are Pauli matrices in two different spaces, attributed to pseudospin and real spin of the considered structure.

Introducing spin index $\sigma = \pm 1$, we can rewrite Eq. (1) in a block-diagonal matrix form

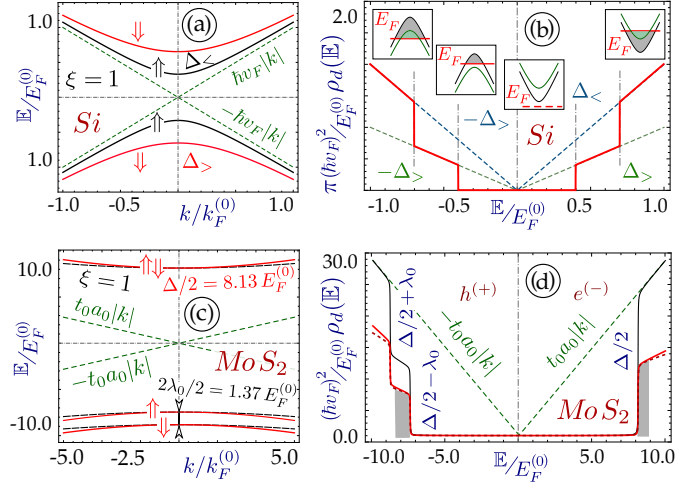


FIG. 1: (Color online) Energy dispersions and density-of-states (DOS) for silicene (upper panels (a) and (b)) and molybdenum disulfide (plots (c) and (d)). Left panels (a) and (c) represent low-energy dispersions in K valley ($\tau = 1$) for both materials. Linear dispersions, corresponding to zero band gap, are also provided for comparison. The range of the wave vector is extended to $\pm 5k_F^{(0)}$ for MoS_2 , in plot (c), in order to display finite curvature of the dispersion curves which is markedly suppressed due to a large band gap parameter $\Delta = 1.9 eV$. The DOS for TMDC's represented in panel (d), is calculated for the gapped graphene approximation, given by Eq. (13), and for a general model (12), which displays substantial difference between the two results.

$$\hat{\mathbb{H}}_{\xi,\sigma} = \begin{pmatrix} -\xi\sigma\Delta_{SO} + \Delta_z & \hbar v_F(k_x - ik_y) \\ \hbar v_F(k_x + ik_y) & \xi\sigma\Delta_{SO} - \Delta_z \end{pmatrix}. \quad (2)$$

The energy dispersions are

$$\varepsilon_{\xi,\sigma}^\gamma(k) = \gamma \sqrt{(\xi\sigma\Delta_z - \Delta_{SO})^2 + (\hbar v_F k)^2}, \quad (3)$$

where $\gamma = \pm 1$ determines the electron or hole state similar to graphene, with a finite or zero band gap. These dispersions, given by Eq. (3), represent two pairs of spin-dependent energy subbands in a chosen valley with the two generally different band gaps $|\Delta_{SO} - \xi\sigma\Delta_z|$, which will be later referred to as $\Delta_{<,>} = |\Delta_{SO} \mp \Delta_z|$. Clearly, both energy gaps depend on the perpendicular electrostatic field and the two subbands corresponding to the $\xi\sigma = \pm 1$ indices switch their locations with increasing field strength. Small or zero \mathcal{E}_z is related to a topological insulator (TI) states with $\Delta_z < \Delta_{SO}$. Once the two gaps become equal, we observe a metallic gapless state with $\Delta_{<} = 0$ and a finite $\Delta_{>}$, defined as valley-spin polarized metal (VSPM). For larger fields, $\Delta_z \sim \mathcal{E}_z$ would always exceed the constant intrinsic spin-orbit gap Δ_{SO} , which corresponds to the standard band insulator (BI) state.

The DOS which is in general defined by

$$\rho_d(\mathbb{E}) = \int \frac{d^2\mathbf{k}}{(2\pi)^2} \sum_{\gamma=\pm 1} \sum_{\xi,\sigma=\pm 1} \delta \left[\mathbb{E} - \varepsilon_{\xi,\sigma}^\gamma(k) \right], \quad (4)$$

is immediately obtained for silicene (see Appendix A) as

$$\rho_d(\mathbb{E}) = \frac{1}{\pi} \sum_{\gamma=\pm 1} \frac{\mathbb{E}}{\hbar^2 v_F^2} \sum_{i=<,>} \Theta \left[\frac{\mathbb{E}}{\gamma} - \Delta_i \right], \quad (5)$$

in terms of the unit step function $\Theta(x)$. We note that for systems sharing the same Dirac cone characteristics with arbitrary energy gap, the DOS is linear analogous to graphene. Experimentally obtained linear V-shaped DOS was used to verify the Dirac cone dispersion for germanene.⁷⁹ However, $\rho_d(\mathbb{E})$ has a finite value only above the energy gap since only for this energy range electronic states exist and that is how the band gap plays an important role.

Finite-temperature chemical potential for an electronic system is obtained using conservation of carrier density n of electrons ($n^{(e)}$) and holes $n^{(h)}$ concentrations at all temperatures, including $T = 0$. In this regard, we have

$$n = n^{(e)} + (-1)n^{(h)} = \int_0^{\infty} d\mathbb{E} \rho_d(\mathbb{E}) f_{\gamma=1}(\mathbb{E}, T) - \int_{-\infty}^0 d\mathbb{E} \rho_d(\mathbb{E}) \{1 - f_{\gamma=1}(\mathbb{E}, T)\}. \quad (6)$$

At zero temperature, the density n is related to the Fermi energy E_F in a straightforward way. If only one subband is occupied, we obtain

$$n = \frac{1}{2\pi} \frac{E_F^2 - \Delta_{<}^2}{\hbar^2 v_F^2}. \quad (7)$$

Alternatively, if the doping density is such that both subbands are populated, then E_F is obtained from

$$n = \frac{1}{\pi} \frac{1}{\hbar^2 v_F^2} \left[E_F^2 - \frac{1}{2} (\Delta_{<}^2 + \Delta_{>}^2) \right], \quad (8)$$

and the critical density required to start filling the upper subband is $n_c = 2\Delta_{SO}\Delta_z/\pi\hbar^2v_F^2$.

We prove in Appendix B that the finite-temperature chemical potential could be obtained from the following equation

$$n \left(\frac{\hbar v_F}{k_B T} \right)^2 = \sum_{\gamma=\pm 1} \frac{\gamma}{\pi} \sum_{i=<,>} -\text{Li}_2 \left\{ -\exp \left[\frac{\gamma\mu(T) - \Delta_i}{k_B T} \right] \right\} + \frac{\Delta_i}{k_B T} \ln \left\{ 1 + \exp \left[\frac{\gamma\mu(T) - \Delta_i}{k_B T} \right] \right\}, \quad (9)$$

where $\text{Li}_2(x)$ is a polylogarithm function. Connecting the doping density n with the Fermi energy through either Eq. (7) or Eq. (8) depending on how many subbands are doped at zero temperature, we derive the chemical potential with a value equal to E_F at $T = 0$, for all accessible temperatures. Although this equation is *transcendental* and cannot be resolved algebraically, a quasi-analytic or one-step numerical solutions could be easily provided for any finite temperature without having to perform an integration.

Clearly, the chemical potential for silicene depends on the energy band gaps Δ_i , $i = <, >$. Our approach, discussed in Appendix B, is valid for a variety of materials with linear energy dependence for the DOS, including MoS_2 . Specifically, Eq. (9) also describes $\mu(T)$ for gapped graphene with two degenerate subbands, or $\Delta_{<} = \Delta_{>} = \Delta_0$. For gapless pristine graphene $\Delta_0 = 0$ and $\pi n = [E_F/(\hbar v_F)]^2$, we have

$$\frac{1}{2(k_B T)^2} E_F^2 = - \sum_{\gamma=\pm 1} \gamma \text{Li}_2 \left\{ -\exp \left[\frac{\gamma\mu(T)}{k_B T} \right] \right\}. \quad (10)$$

If the temperature is low with $k_B T \ll E_F$, Eq. (10) is reduced to the expressions, derived in Refs. [70,73] and [80].

All our considered materials could be effectively classified by the existing or broken symmetries of certain kinds, and, consequently, by the degeneracy of their energy subbands, which may be generally different for electrons and holes. In this respect, graphene represents the simplest case with a fourfold spin and valley degeneracy of $\pm\sqrt{(\hbar v_F k)^2 + \Delta_0^2}$ states. Silicene and germanene dispersions, yet showing complete electron/hole symmetry, exhibit spin- and valley-dependent pairs of subbands, each being double degenerate. Finally, MoS_2 demonstrates broken symmetry between its electrons and holes, and a finite energy separation between two non-equivalent holes subbands.

Typical energy dispersions and DOS for silicene and molybdenum disulfide are presented in Fig. 1. For both materials, we consider the K valley with $\xi = 1$ so that the upper electron and lower hole subbands correspond to $\sigma = 1$ spin. Every time a new subband, or their degenerate manifold, begins to be doped, we see an immediate increase, or discontinuity, of the DOS, as schematically shown for silicene in the insets of Fig. 1 (b). It is important to observe that for both silicene and gapped graphene, $\rho_d(\mathbb{E})$ is directly proportional to energy \mathbb{E} , i.e., the DOS for Dirac materials with finite and zero gap are exactly the same as long as we measure it above the energy band gap. With no electronic states inside the gap region, we have $\rho_d(\mathbb{E} < 0) = 0$.

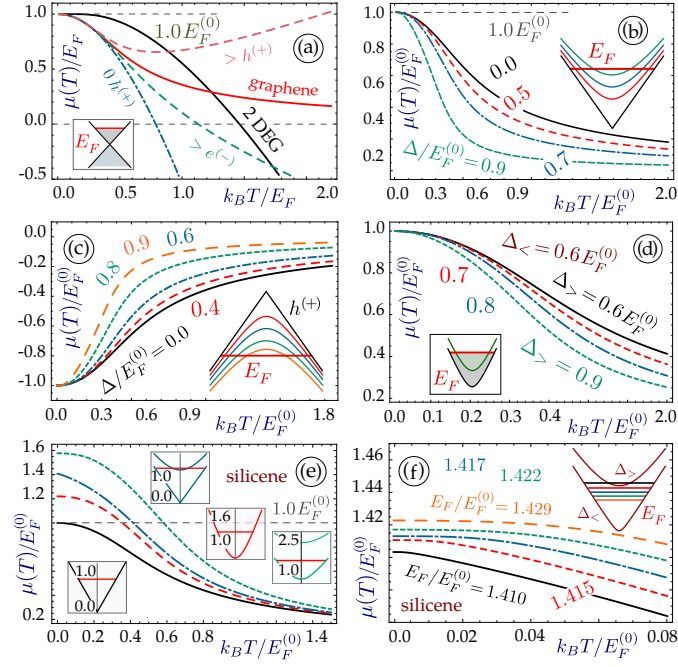


FIG. 2: (Color online). Finite temperature chemical potential $\mu(T)$ for graphene and silicene. Panel (a) shows $\mu(T)$ dependence for a number of representative cases - 2DEG with $\varepsilon \sim k^2$, $\rho_d(\mathbb{E}) = \text{const}$ and no holes (black solid line), gapless graphene with $\rho_d(\mathbb{E}) \sim \mathbb{E}$ (solid red curve) and three others with broken electron-hole symmetry. Dash-dotted blue line describes graphene without holes $\rho_d^{(h)}(\mathbb{E} < 0) = 0$, green dashed curve corresponds to graphene with reduced hole DOS $\rho_d^{(h)}(\mathbb{E} < 0) = 1/2 \rho_d^{(e)}(\mathbb{E} > 0)$, and the watermelon dashed line shows the opposite situation, i.e., reduced electron DOS $\rho_d^{(e)}(\mathbb{E} < 0) = 1/2 \rho_d^{(e)}(\mathbb{E} > 0)$. Plots (b) and (c) present $\mu(T)$ for gapped graphene for electron and hole doping, respectively, for chosen Fermi energy. Each curve is matched to a specific energy gap, as described schematically in the insets. Chemical potential for silicene with both subbands filled $\Delta_< = 0.6 E_F^{(0)}$ and different $\Delta_>$ is presented in panel (d). Black curve describes $\Delta_> = \Delta_< = 0.6 E_F^{(0)}$ (gapped graphene), red and short-dashed line - $\Delta_< = 0.7 E_F^{(0)}$, dotted blue line - $\Delta_< = 0.8 E_F^{(0)}$ and dashed green curve corresponds to $\Delta_< = 0.9 E_F^{(0)}$. Plot (e) combines two degenerate-subband situations - graphene ($\Delta_{SO} = \Delta_z = 0.0$ and, $E_F = E_F^{(0)}$), black solid curve and gapped graphene with $\Delta_{SO} = 0.7 E_F^{(0)}$, $\Delta_z = 0.0$ and $E_F = 1.22 E_F^{(0)}$ (red dashed curve) with the two cases of silicene with split subbands - $\Delta_{SO} = \Delta_z = 0.7 E_F^{(0)}$ and $\Delta_z = 0.7 E_F^{(0)}$, $E_F = 1.41 E_F^{(0)} \gtrsim \Delta_>$, and, finally, $\Delta_{SO} = 0.7 E_F^{(0)}$, $\Delta_z = 1.4 E_F^{(0)}$ and $E_F = 1.58 E_F^{(0)}$. The subband schematics and the Fermi level for each case are given in the insets. Panel (f) shows $\mu(T)$ at low temperatures satisfying $k_B T \leq 0.1 E_F^{(0)}$ for a number of cases of doping level located close to the upper subband $\Delta_> \approx E_F$. Here, $\Delta_{SO} = 0.7 E_F^{(0)}$ for each curve, $\Delta_z = 0.70, 0.75, 0.80$ and $0.85 E_F^{(0)}$, while the Fermi levels at $T = 0$ are 1.410, 1.415, 1.417, 1.422 and 1.428 $E_F^{(0)}$.

In Fig. 2, we display our results for the finite-temperature chemical potential for graphene and buckled honeycomb lattices. First, we show how dissimilar this temperature dependence might be for various electronic systems. In Fig. 2 (a), this situation is described for a 2DEG with a parabolic energy band and constant DOS, graphene with $\rho_s(\mathbb{E}) \sim \mathbb{E}$, as well as two *model structures* - graphene with no hole states, with doubly prevailing electrons $\rho_d(\mathbb{E} > 0) = 2\rho_d(\mathbb{E} < 0)$ and doubly prevailing hole DOS. At low temperatures, all the curves, except the one for the 2DEG, are nearly identical since the holes do not play any important role. The hole distribution function is complimentary to that for electrons, i.e., $1 - f_e(\epsilon) \rightarrow 0$, and, therefore, inconsequential. However, when the temperature becomes comparable with the Fermi energy, the hole thermal excitations become crucial, causing an opposite effect compared with that for electrons. They mitigate the reduction of the chemical potential and eventually prevent $\mu(T)$ from crossing the zero energy level. This is seen particularly well for a hole-dominating system ($> h^{(+)}$), for which the chemical potential starts to increase and ultimately exceeds the initial E_F value. We conclude that only total electron/hole symmetry, but not the energy gap, keeps the chemical potential positive for arbitrary high temperatures.

For the remaining plots, we consider the behavior of $\mu(T)$ for graphene and silicene with different gaps. At $T = 0$, we may keep the Fermi energy fixed so that the actual electron density n differs, in which case the states with a larger gap receive much smaller amount. Alternatively, we can dope the sample and $\mu(T)$ shows much stronger reduction, or we can fix the carrier density n so that the Fermi energy increases in the case with larger gap (see Eq. (7)). The former case is shown in panels (b), (c) and (d), whereas the latter at (e) and (f). In general, the carrier density n is

accepted to be the most meaningful parameter, determining the Fermi energy for each specific system.

Plots (b) and (c) are designed to demonstrate complete reflection symmetry of the chemical potential between electron and hole doping for all energy band gaps. This is a manifestation of $\gamma = \pm 1$ symmetry of these states persisting at arbitrary temperatures. Silicene with both filled subbands exhibits qualitatively similar finite-temperature behavior as gapped graphene. More generally, only the actual gaps are relevant, but not the exact type of states (such as topological insulator or regular band insulator), or the way in which such a state has been achieved.

We now pay attention to the following situation in silicene. At $T = 0$, the Fermi level is chosen so that only the lower subband is filled. In contrast, the upper one $\Delta_>$ is located so close to the Fermi level E_F , that it starts getting populated at all, even very small temperatures. Thermally-induced doping, received by the $\Delta_>$ -subband, results in a much stronger reduction rate of $\mu(T)$, as shown in Fig. 2 (e). Such situation suggests very special thermal properties of silicene with closely located energy subbands, and shares this behavior with graphene having an additional spin and valley degeneracy. We investigate this phenomenon even further by adjusting the upper subband in the vicinity of the Fermi level, as shown in Fig. 2 (f). Now, each $\mu(T)$ curve demonstrates a significantly pronounced decrease whenever the upper subband filling becomes essential. These two different types of $\mu(T)$ behavior in silicene could be used to achieve its additional tunability by introducing the upper energy subband $\Delta_>$.

B. Transition metal dichalcogenides

The low-energy electronic states in monolayer molybdenum disulfide (MoS_2 , ML-MDS), a prototype transition metal dichalcogenide, could be effectively described by a *two-band* model Hamiltonian^{32,34,38}

$$\hat{\mathbb{H}}_d^{\xi,\sigma} = \left(\frac{1}{2} \xi \sigma \lambda_0 + \frac{\hbar^2 k^2}{4m_e} \alpha \right) \hat{\mathbb{I}}_{2 \times 2} + \left(\frac{\Delta}{2} - \frac{1}{2} \xi \sigma \lambda_0 + \frac{\hbar^2 k^2}{4m_e} \beta \right) \hat{\Sigma}_z + t_0 a_0 \hat{\Sigma}_\xi \cdot \mathbf{k}, \quad (11)$$

whose important feature is a major gap parameter $\Delta = 1.9 \text{ eV}$ which results in the actual band gap $\simeq 1.7 \text{ eV}$, large compared to that for silicene. The spin-orbit coupling parameter $\lambda_0 = 0.042 \Delta$ represents a smaller, but essential correction, to the single-particle excitation spectrum and the band gap. The energy subbands are now spin- and valley- dependent since the corresponding degeneracy is lifted. The electron hopping parameter $t_0 = 0.884 \Delta$ and $a_0 = 1.843 \text{ \AA}$ shape the Dirac cone term in the Hamiltonian Eq. (11) as $t_0 a_0 = 4.95 \times 10^{-29} \text{ J}\cdot\text{m}$, counting up to ≈ 0.47 of $\hbar v_F$ value in graphene.

Next, we include the $\simeq k^2$ mass terms with $\alpha = 2.21 = 5.140 \beta$ in which m_e is the free electron mass. Our considered values of Fermi momentum at zero temperature are determined by the experimentally allowed electron and hole doping densities $n = 10^{14} \div 10^{16} \text{ m}^{-2}$ as $k_F = \sqrt{\pi n} \simeq 10^8 \div 10^9 \text{ m}^{-1}$.¹⁰³ Anisotropic trigonal warping term $t_1 a_0^2 (\hat{\Sigma}_\xi \cdot \mathbf{k}) \hat{\sigma}_x (\hat{\Sigma}_\xi \cdot \mathbf{k})$ is clearly beyond our consideration since $\simeq t_1 = 0.1 \text{ eV} = 0.053 \Delta$ term does not cause any effect on the electron dispersions. The energy dispersion relations, corresponding to the Hamiltonian Eq. (11)

$\varepsilon_\gamma^{\xi,\sigma}(k) = \varepsilon_0^{\xi,\sigma}(k) + \gamma \sqrt{\left[\Delta_0^{\xi,\sigma}(k) \right]^2 + (t_0 a_0 k)^2}$, formally represent *gapped graphene* with a k -dependent gap term $\Delta_0^{\xi,\sigma}(k) = \hbar^2 k^2 \beta / (4m_e) + \Delta / 2 - \xi \sigma \lambda_0 / 2$, and a band shift $\varepsilon_0^{\xi,\sigma}(k) = \hbar^2 k^2 \alpha / (4m_e) + \xi \sigma \lambda_0 / 2$.^{38,81}

Neglecting only the $\mathcal{O}(k^4)$ terms leads us to

$$\varepsilon_\gamma^{\xi,\sigma}(k) \simeq \frac{1}{2} \xi \sigma \lambda_0 + \frac{\alpha \hbar^2}{4m_e} k^2 + \frac{\gamma}{2} \left\{ \left[(2t_0 a_0)^2 + (\Delta - \xi \sigma \lambda_0) \beta \hbar^2 / m_e \right] k^2 + (\Delta - \xi \sigma \lambda_0)^2 \right\}^{1/2}. \quad (12)$$

This is the principal model which we will use to describe the energy dispersions of MoS_2 in our work. The $\simeq k^4$ terms, trigonal warping and anisotropy are considered to be non-essential, even though as we will later see, cause certain discrepancies in the DOS.¹⁰⁴ We also show (see Appendix A) that the curvature of the energy subbands in TMDC's is so small that even the highest possible doping density 10^{17} m^{-2} results in the Fermi energies $\simeq \lambda_0$. Thus, at zero or low temperatures, we do not need to consider any high-energy corrections to Eq. (12). On the other hand, inclusion of higher order terms into the dispersions, would enormously complicate the DOS calculation.

At high temperatures, the electronic states far from the Dirac point would also receive substantial temperature-induced doping density due to the so-called Fermi tail.⁸⁰ In that case, our model Hamiltonian in Eq. (11) and especially, simplified dispersion relation (12) would no longer provide a satisfactory approximation. Consequently, our primary focus is on *small but finite temperatures* for which the initial doping density and E_F still play an important role, beyond the $\mathcal{O}(T^2/T_F^2)$ approximation discussed in Ref. [70].

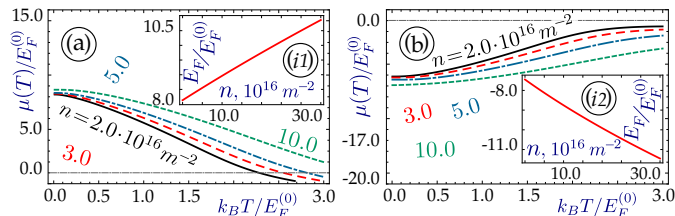


FIG. 3: (Color online). Temperature-dependent chemical potential for MoS_2 . Panel (a) presents the $\mu(T)$ dependence for various initial *electron* doping densities - $n = 2.0 \cdot 10^{16} m^{-2}$ (black solid line), $n = 3.0 \cdot 10^{16} m^{-2}$ (red and dashed), $n = 5.0 \cdot 10^{16} m^{-2}$ (dotted blue curve) and $n = 1.0 \cdot 10^{17} m^{-2}$ (green short-dashed line). Plot (b) shows the corresponding dependence for *hole* doping with the same densities. Insets (i1) and (i2) illustrates how the Fermi energy depends on the electron and hole doping densities at zero temperature.

Here we note that for MoS_2 , similar to the buckled honeycomb lattices, spin and valley indices always appear together as a product, so that taking into account a $\times 2$ degeneracy, a single composite index $\nu = \xi\sigma$ could be effectively introduced. We are going to use only the index ν for the rest of our consideration. A valley- and spin-resolved gapped graphene approximation of dispersions (12) arises once we also neglect the mass terms in Eq. (12)

$$\varepsilon_\gamma^\nu(k) \simeq \nu\lambda_0/2 + \gamma\sqrt{(t_0a_0)^2k^2 + (\Delta - \nu\lambda_0)^2/4}. \quad (13)$$

This approximation has a few important advantages including simplicity and its formal resemblance with gapped graphene so that all the crucial quantities such as the DOS, wave function, polarizability and many others are already known. Furthermore, it gives a quite a suitable description of the energy band structure of MoS_2 , taking into account a large gap parameter and ν -dependent splitting of the two hole subbands. Nevertheless, the mass terms must be taken into account for a proper evaluation of the DOS and most of the temperature-dependent properties of TMDC's. As we demonstrated in Appendix A, even in the simplest possible parabolic subbands approximation, valid only for small wave vectors $k \rightarrow 0$, the mass terms make a contribution, comparable with the Dirac cone and band gap parts of Hamiltonian (11). Very small curvature of the energy subbands, mentioned above results in a tremendous $\rho_d \sim m_{eff}$, so that even $\simeq \alpha/(4m_e)$ correction, hardly noticeable on the electron band structure, becomes significant. It basically discards the DOS results obtained from the gapped graphene model, even at zero or small wave vectors. Importance of the mass and even higher order terms for the plasmon calculation was discussed in Ref. [38].

Taking into account all the required terms in (11), rigorous numerical calculations give accurate results for the electron DOS for MoS_2 . In Fig. 1 (d), we present all three possible outcomes. Based on the gapped graphene model, the DOS is nearly twice as large as its numerical values. ^{81,83} In contrast, our $\sim k^2$ model (12) demonstrates quite a good match, especially in the low-energy range. We also note that the numerically obtained dependence is clearly linear for a wide range of energies, much exceeding our considered diapason.

In summary, we consider a piecewise linear approximation $\rho_d(\mathbb{E})$ relatively close ($\delta\mathbb{E} \simeq \lambda_0$) for each of the three non-degenerate subbands $\rho_d(\mathbb{E}) = c_0^{(i)} + c_1^{(i)} \mathbb{E}$ and $\rho_d(\mathbb{E}) = 0$ in the gap region $-\Delta/2 + \lambda_0 < \mathbb{E} < \Delta/2$. The expansion coefficients are obtained as $c_0^{(1)} = 2.837 E_F^{(0)}/(\hbar v_F)^2 = 0.043 t_0^{-1} a_0^{-2}$, $c_1^{(1)} = -1.397 (\hbar v_F)^{-2} = -0.308 (t_0 a_0)^{-2}$ for $\gamma = -1$, $\nu = -1$ and $-\Delta/2 - \lambda_0 \geq \mathbb{E} \leq -\Delta/2 - \lambda_0$. Finally, when $\gamma = -1$, but $\nu = 1$ and $\mathbb{E} \leq -\Delta/2 + \lambda_0$, the hole DOS coefficients are $c_0^{(2)} = 1.132 E_F^{(0)}/(\hbar v_F)^2 = 0.0174 t_0^{-1} a_0^{-2}$, $c_1^{(2)} = -0.767 (\hbar v_F)^{-2} = -0.169 (t_0 a_0)^{-2}$. For electrons with $\gamma = +1$ at $\mathbb{E} = \Delta/2 + \delta\epsilon$, the two quasi-degenerate subbands lead to the DOS equal to $c_0^{(3)} = 5.110 E_F^{(0)}/(\hbar v_F)^2 = 0.078 t_0^{-1} a_0^{-2}$ and $c_1^{(3)} = 0.815 (\hbar v_F)^{-2} = 0.179 (t_0 a_0)^{-2}$.

We adopt these values for $\rho_d(\mathbb{E})$, which arise from the numerical calculations in order to achieve the highest possible precision and credibility for our finite-temperature derivations. However, our effective model, presented in Appendix A, gives the DOS results which show good agreement with these numerical values and could be used for decisive estimates for various collective calculations for MoS_2 .

Once the DOS is known, we are in a position to calculate the Fermi energy for a given doping density $n_{(0)}^e$. The new point here is that $\rho_d(\mathbb{E})$ is not directly proportional to the energy so that E_F is determined by

$$n_{(0)}^e = \left(E_F - \frac{\Delta}{2} \right) \left[c_0^{(3)} + \frac{c_1^{(3)}}{2} \left(\frac{\Delta}{2} + E_F \right) \right], \quad (14)$$

or

$$E_F^{(e)} = \frac{1}{2c_1^{(3)}} \left\{ -2c_0^{(3)} + \left[\left(2c_0^{(3)} + c_1^{(3)} \Delta \right)^2 + 8n_{(0)}^e c_1^{(3)} \right]^{1/2} \right\}. \quad (15)$$

For hole doping, the Fermi energy differs from the previously considered electron doping case, i.e.,

$$E_F^{(h)} = \frac{1}{c_1^{(2)}} \left\{ -c_0^{(2)} + \left\{ -2c_1^{(2)} n_{(0)}^h + \left[c_0^{(2)} - c_1^{(2)} \left(\frac{\Delta}{2} - \lambda_0 \right) \right]^2 \right\}^{1/2} \right\} \quad (16)$$

Numerically, our results for the Fermi energy for electrons and holes are presented in insets (i1) and (i2) of Fig. 3. Here, both linear and quadratic terms in the doping density equations are present (see Eq. (14)), and, most importantly, *there is no symmetry* between the electron and hole states. Unlike graphene, the linear dependence here dominates for both cases due to the large energy band gap. Each curve starts from the corresponding band gap - $\Delta/2 = 8.13 E_F^{(0)}$ for electrons and $-\Delta/2 + \lambda_0 = -7.45 E_F^0$. The corresponding well-known result for gapped graphene $E_F^2 - \Delta_0^2 = 2\pi n (\hbar v_F)^2$ are verified by putting $c_1^{(i)} \rightarrow 0$ and $\lambda_0 \rightarrow 0$.

The finite-temperature chemical potential for MoS_2 is obtained in a similar way, as we have done for the buckled honeycomb lattices, except that we need to evaluate *four* different terms related to the two separate hole subbands (see Eq. (B26)). The corresponding numerical results are described in Fig. 3. As discussed above, the most special property of TMDC's is the broken electron/hole symmetry. Consequently, the chemical potential for the electron doping becomes negative at $T \approx 2.5 E_F$, while $\mu(T)$ for hole doping does not ever change its sign. Broken electron/hole symmetry leads to two substantially different types of temperature dependence of the chemical potential. Thus, MoS_2 represents a special material with unique symmetry properties and chemical potential dependence, so far encountered only in certain types of semiconductors but not in Dirac materials.

III. PLASMON EXCITATIONS AT FINITE TEMPERATURE

As one of the most relevant applications of our finite-temperature chemical potential formalism, we briefly consider plasmons for an extrinsic, substantially doped at $T = 0$, free-standing gapped Dirac cone material. The plasmon dispersion relation is calculated from the zeros of the dielectric function $\epsilon(q, \omega)$, expressed in the random phase approximation (RPA) as

$$\epsilon(q, \omega) = 1 - v(q) \Pi_T(q, \omega | \mu(T), T, \Delta_i) = 0, \quad (17)$$

where $v(q) = 2\pi e^2 / (\epsilon_s q)$ is the Fourier-transformed two-dimensional Coulomb potential, and $\epsilon_s = 4\pi\epsilon_0\epsilon_r$ with ϵ_b is the background dielectric constant in which the 2D material is embedded. At finite temperature, the dynamical polarization function Π_T is given as an integral transformation⁸⁴ of its $T = 0$ counterpart Π_0 , i.e.,

$$\Pi_T(q, \omega | \mu(T), T, \Delta_i) = \frac{1}{2k_B T} \int_0^\infty d\xi \frac{\Pi_0(q, \omega | \xi, \Delta_i)}{1 + \cosh \{ [\mu(T, E_F) - \xi] / (k_B T) \}} \quad (18)$$

The evaluation of the zero-temperature polarizability is quite similar for buckled honeycomb lattices and MoS_2 , since in both cases their low-energy bandstructure is represented by two generally inequivalent double-degenerate pairs of subbands which depend on the composite index $\nu = \sigma \xi$. For any such pair, $\Pi_0^{(\nu)}$ is obtained in the one-loop approximation ($g_0 = 2$) as

$$\Pi_0^{(\nu)}(q, \omega | E_F, \Delta_\nu) = \frac{g_0}{8\pi^2} \int d^2 k \sum_{\gamma, \gamma' = \pm 1} \left(1 + \gamma \gamma' \frac{\mathbf{k} \cdot (\mathbf{k} + \mathbf{q}) + \Delta_\nu^2}{\varepsilon^\nu(k) \varepsilon^\nu(|\mathbf{k} + \mathbf{q}|)} \right) \frac{f[\mathbb{E} - \varepsilon_\gamma^\nu(k)] - f[\mathbb{E} - \varepsilon_{\gamma'}^\nu(|\mathbf{k} + \mathbf{q}|)]}{\varepsilon_\gamma^\nu(k) - \varepsilon_{\gamma'}^\nu(|\mathbf{k} + \mathbf{q}|)}, \quad (19)$$

where $f[\mathbb{E} - \gamma \varepsilon_\nu(k)]$ is the Fermi-Dirac distribution function, showing electron and hole occupation numbers for chosen energy \mathbb{E} . At $T = 0$, it is a Heaviside unit step function $\Theta[\mathbb{E} - \varepsilon_\gamma^\nu(k)]$. We note that the extra 1/2 comes from

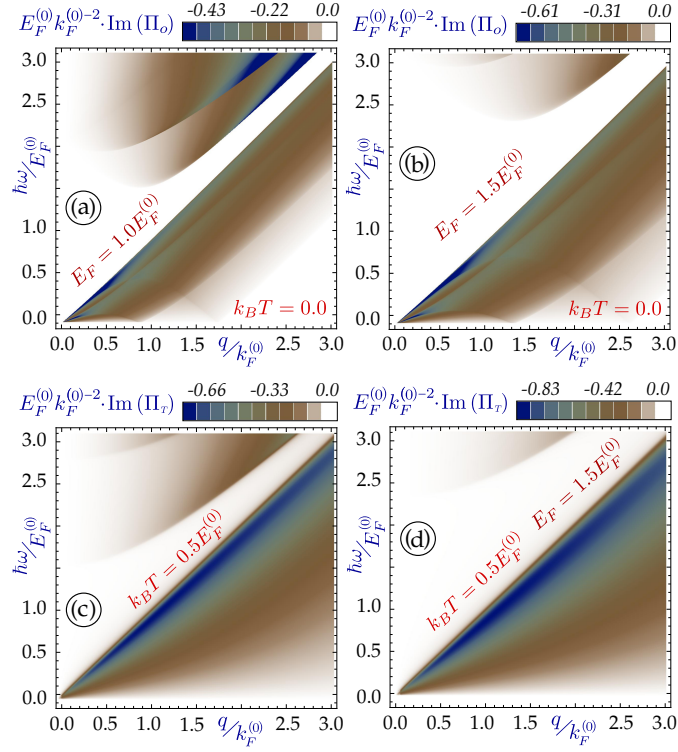


FIG. 4: (Color online) Single-particle excitation regions or particle-hole modes, outlined by non-zero $\text{Im } \Pi_T(q, \omega)$ at an arbitrary temperature for silicene with $\Delta_{SO} = 0.7 E_F^{(0)}$ and $\Delta_z = 0.2 E_F^{(0)}$. The upper panels (a) and (b) describe the situation for zero temperature, while the lower plots (c) and (d) were obtained for $T = 0.5 E_F^{(0)}$. Left panels (a) and (c) are for a system with $E_F = 1.0 E_F^{(0)}$ whereas the right ones - with $E_F = 1.5 E_F^{(0)}$. Alternatively, the regions of $\text{Im } \Pi_T(q, \omega) = 0$ specify plasmon excitations with no Landau damping.

the form factor $1/2[1 + \gamma\gamma' \dots]$ which also depends on the absolute value of each energy $\varepsilon^\nu(k) = 1/\gamma \varepsilon_\gamma^\nu(k)$. We also note that since any valley or spin transitions are inadmissible and only one summation over the index ν is included, compared to the electron/hole indices γ and γ' . Thus, for both types of materials, the dynamical polarization function is obtained as a sum of terms obtained from Eq. (19) over ν ¹⁷

$$\Pi_0(q, \omega | E_F, \Delta_i) = \sum_{\nu} \Pi_0^{(\nu)}(q, \omega | E_F, \Delta_\nu). \quad (20)$$

Our results for the polarization functions and plasmon excitations are presented in Figs. 4 and 5.

First, we need to address the imaginary part of the polarizability since it specifies the regions and intensity of the plasmon damping. We see that at a finite temperature the plasmon dissipation generally increases and the damping-free regions are nearly absent. Once the temperature becomes high, the imaginary part of the polarization function is reduced as $1/T$,^{70,80} so there is no uniform temperature dependence of the plasmon damping. Doping and proportional increase of the energy band gaps, in contrast, increase the regions free of single-particle excitation spectrum (see Fig. 4 (b)), so the effect of a finite temperature and E_F on the plasmon dissipation could be opposite. The real part of $\Pi_0(q, \omega | E_F, \Delta_i)$, shown in Fig. 5 (a)-(d), designates the location and slope of the corresponding plasmon branches which are presented in panels (e) and (f). Here, the temperature and the doping produce a similar effects, shifting the location of the peaks to the right. The real part of the polarization function must be positive in order to enable a real solution of Eq. (17) Plasmon branches are located at higher energies for a given wave vector due to either an initial increase of the Fermi energy or thermally-induced doping.

A. Non-local plasmons in an open system

Concluding our investigation of extrinsic 2D materials, we now turn to the plasmon excitations in so-called 2D open systems (2DMOS). Such a nanoscale hybrid arrangement being a part of graphene-based nanoscale devices,^{85,86}

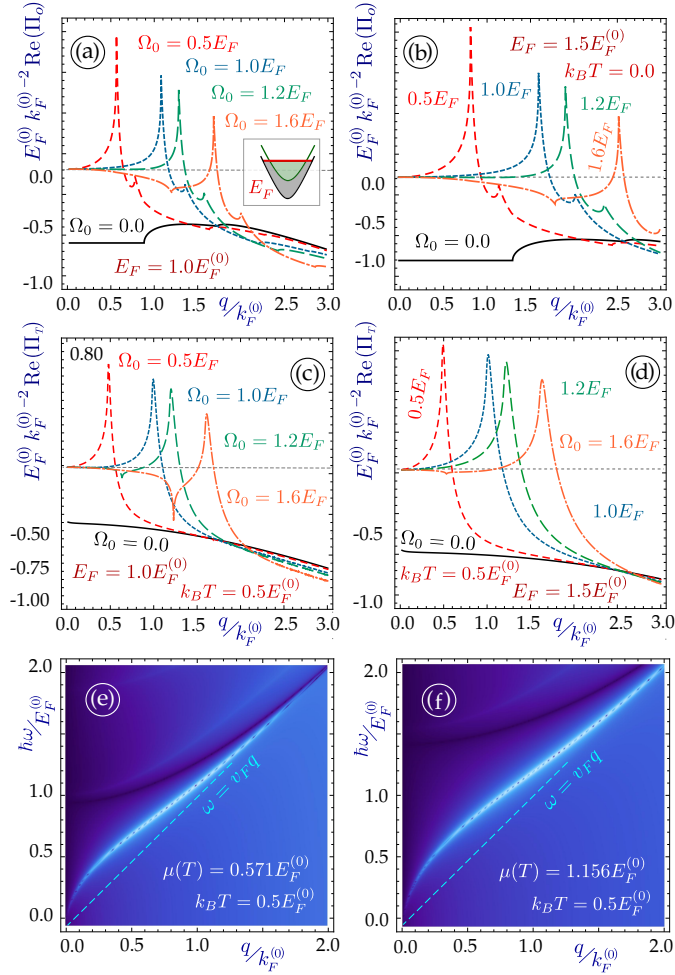


FIG. 5: (Color online) Dynamic polarization function and plasmon excitations for silicene with $\Delta_{SO} = 0.7 E_F^{(0)}$ and $\Delta_z = 0.2 E_F^{(0)}$. Panels (a) - (d) present constant frequency cuts of $\text{Re} \Pi_T(q, \omega)$ as a function of q for $\Omega_0 = 0.0, 0.5, 1.0, 1.2$ and $1.6 E_F^{(0)}/\hbar$, described by solid black, dashed red, short-dashed blue, long-dashed green and dash-dotted orange lines, respectively, for each plot. Panels (a) and (b) show the zero temperature case, (c) and (d) - $T = 0.5 E_F^{(0)}$. Initial ($T = 0$) doping is chosen to yield $E_F = 1.0 E_F^{(0)}$ for plots (a) and (c) while panels (b) and (d) present the case of $E_F = 1.5 E_F^{(0)}$. Plasmon dispersions at $T = 0.5 E_F^{(0)}/k_B$ for $E_F = 1.0 E_F^{(0)}$ is represented in plot (e), and for $E_F = 1.5 E_F^{(0)}$ - in panel (f).

consists of a 2D layer (it could be 2DEG, graphene, a buckled honeycomb layer, or MoS_2), which is Coulomb coupled (not chemically bound) with a semi-infinite conductor and its surface plasmon.^{87,88} While a plasmon excitation in a closed system is determined by two-particle Greens functions, in 2DMOS it more involved, depending on the Coulomb interaction with the environment.^{89,90} The important feature of such a system is the screened Coulomb coupling between the electrons in graphene and the conducting substrate.⁴² Such a screened potential could be obtained using the nonlocal frequency-dependent inverse dielectric function⁹¹⁻⁹⁴ Consequently, two⁸⁸ or more⁹⁵ linear plasmon branched have been obtained, confirming some previous experimental claims.^{64,96} For finite temperature, their coupling to an external reservoir is reflected in existence of extra plasmon dissipation channels.⁸⁰

The plasmon branches in such system are obtained as zeros of a so-called structure factor $S(q, \omega | \mu(T), \Delta_i)$, playing the role of the dielectric function $\epsilon(q, \omega)$ in an isolated layer. It is obtained as^{80,88}

$$S(q, \omega | \mu(T), \Delta_i) = 1 - v(q) \Pi^{(0)}(q, \omega; \mu) \left\{ \frac{1 - \epsilon_B(\omega)}{1 + \epsilon_B(\omega)} \text{Exp}(-2aq) + 1 \right\}, \quad (21)$$

where a is the distance between the 2D layer and the surface and the bulk dielectric function is given in the local limit as $\epsilon_B = 1 - \Omega_p^2/\omega^2$. The bulk-plasma frequency, defined as $\Omega_p^2 = (n_m e^2)/(\epsilon_o \epsilon_S m^*)$, depends on on the electron

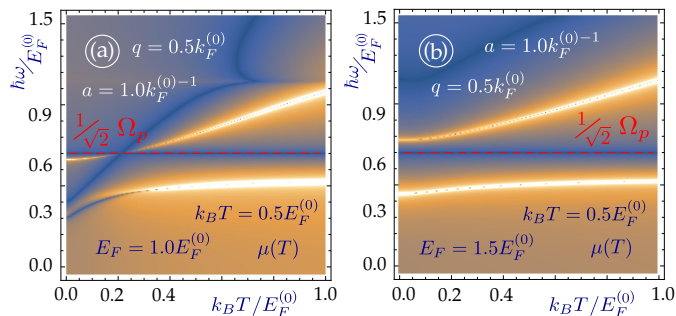


FIG. 6: (Color online) Temperature-dependent non-local plasmon excitations for a silicene-based hybrid system with $\Delta_{SO} = 0.7 E_F^{(0)}$ and $\Delta_z = 0.2 E_F^{(0)}$. Density plots of the real part of $\mathbb{S}_c(T, \omega + 0^+)$ for a constant wave vector $q = 0.3k_F^{(0)}$ are presented, so that the sought low-damped plasmons correspond to their peaks. Panel (a) corresponds to an intrinsic system with no zero-temperature doping, while plot (b) is related to $E_F = 2.0 E_F^{(0)}$.

concentration n_m , its effective mass m^* and the substrate dielectric constant ϵ_S . This approximation stays valid for a large range of wave vectors $q \ll 2 \times 10^9 m^{-1}$ since the Fermi wavelength in metals is comparable with the inverse lattice constant. As a result the frequency of the upper plasmon branch in our system, equal to $\Omega_p/\sqrt{2}$ at $q_{||} \rightarrow 0$, might range from ultra violet down to infrared or even terahertz, depending on the substrate material and must stay commensurate with the energy band gap in the 2D layer.

Previously, we reported that⁸¹ in case of spin- and valley-dependent single-particle excitations in a 2D layer (which is true for buckled honeycomb lattices and MoS_2), such a hybrid structure could be effectively used to directly measure the dielectric properties or spin-orbit coupling parameters of such a layered material because the location of each plasmon branch, its damping rate and the signatures of the particle-hole modes are independently determined by the material parameters of the 2D layer. Each of these properties is unique (for example, the two plasmon branches in silicene-based TDMOS depends on the energy band gaps as $\Delta_i^{1/2}$ and $\Delta_i^{1/4}$, while the outermost PHM boundaries are determined solely by the lower gap $\Delta_<$), so that an additional linear plasmon branch provides us with the required earlier unknown piece of information about the specific material. This is not possible in the case of a single plasmon branch in an isolated layer.

In the present work, we additionally introduce finite doping and temperature into this consideration. Our numerical results for the non-local plasmons for an extrinsic system are presented in Fig. 6. We see that the location and damping of both branches substantially changes in the presence of an initial Fermi energy. At low temperature, this increase is especially apparent, similar to plasmons in an isolated layer. For a sample with stronger doping, $E_F = 1.5 E_F^{(0)}$ at zero temperature, the upper plasmon branch is always located above the surface plasmon level $\Omega_p/\sqrt{2}$ and is never damped.

IV. CONCLUDING REMARKS

We have carried out an extensive investigation of extrinsic, or doped, Dirac gapped materials at arbitrary finite temperatures and obtained a set of algebraic analytic equations determining the chemical potential. Our considered systems include graphene, with or without an energy band gap, buckled honeycomb lattices with spin- and valley-dependent energy subbands and reduced degeneracy, as well as the transition metal dichalcogenides having broken symmetry between the electron and hole states. Our results could also be used to predict the finite-temperature chemical potential for parabolic or quasi-parabolic eigenstates in semiconductors with light or heavy holes.^{97,98} In general, our model is limited only by the linear dependence of the DOS which stays valid over a wide energy range for all the above mentioned materials.

We have demonstrated that the chemical potential depends substantially on the energy band gap(s) of the considered system since the DOS depends on the curvature of each subband. Specifically, we investigated structures with two non-degenerate, separated spin- and valley- resolved energy subbands in both valence and conduction bands, such as silicene. The upper subband would receive thermally-induced doping even if it is undoped at zero temperature. This is always reflected in a higher reduction rate of the chemical potential whenever the second subband doping starts playing a role. Consequently, one can tune the $\mu(T)$ dependence around any required temperature by bringing initial doping close to the higher-energy subband. The number of such separated subbands contributing to the DOS could

be arbitrarily large for an electron in a quantum well or quasi-one-dimensional nanoribbons,⁹⁹ and all these cases could be effectively treated by our model.

The behavior of the chemical potential depends on whether there is symmetry between the electron and hole states in the system. If the DOS for the electrons and holes is equal or symmetric around the Dirac point, then the chemical potential does not change its sign even for high temperatures, i.e., it remains positive for electron doping or stays negative if $E_F < 0$. In fact, these two types of doping result in symmetric behavior, decreasing $|\mu(T)|$, so that the electron-hole symmetry persists at any finite temperature. Let us discuss the electron doping in more detail. Once the temperature is sufficiently high, the hole states become thermally excited and it has an opposite effect to that of electron, decreasing the reduction of the chemical potential. At extremely high temperatures, the two processes have almost equivalent effects and $\mu(T)$ asymptotically tends to zero and never crosses the Dirac point. This situation changes if the DOS of the electron and holes differs and the two hole subbands are energetically not equivalent, as we observe for TMDC's. We have shown that for MoS₂ the chemical potential becomes negative, changing its sign at $T \simeq 2.5E_F$. Alternatively, $\mu(T)$ could never reach the zero energy line if there is hole doping at zero temperature and starts decreasing at sufficiently high temperatures.

As a necessary intermediate step in our derivations, we obtained a piecewise-linear model for the DOS for transition metal dichalcogenides, directly from the Hamiltonian parameters of the considered system. This model gives exact results for $\rho_d(\mathbb{E})$ at the band edges (next to each energy gap) and a fairly good approximation at higher energies. This model significantly improves the results obtained from the spin- and valley-resolved gapped graphene approximation.

Finally, we considered the way in which the initial doping affects the plasmon dispersions $(\hbar\Omega_p/E_F)^2 \simeq \Lambda q$, and the effective length Λ depends on the doping. There could be an initial carrier density at $T = 0$, and the thermally-induced one at finite temperature. The latter doping type results in a finite polarization function and \sqrt{qT} plasmon dispersions even for intrinsic systems.⁷⁰ We demonstrate how much each type of doping contributes this effective length.

Several many-body calculations or collective electronic models requires reliable knowledge of the chemical potential at finite temperature. In the absence of such information, much attention has been directed towards intrinsic, or undoped systems, or low temperatures, so that $\simeq (T/T_F)^2$ series expansions could have been applied. Our results are going to provide considerable assistance in transport studies, optical, thermally modulated conductivity for the materials, discussed in our paper. Consequently, we expect our work to provide an important contribution to electronics, transport and plasmonics of these recently discovered structures, both theory and experiment.

Acknowledgments

D.H. would like to thank the support from the Air Force Office of Scientific Research (AFOSR).

Appendix A: Density-of-states

The DOS for electrons and holes with energy dispersion $\varepsilon_\gamma^{\xi,\sigma}(k)$ is defined as

$$\rho_d(\mathbb{E}) = \int \frac{d^2\mathbf{k}}{(2\pi)^2} \sum_{\gamma=\pm 1} \sum_{\xi,\sigma=\pm 1} \delta[\mathbb{E} - \varepsilon_\gamma^{\xi,\sigma}(k)], \quad (\text{A1})$$

where $\xi = \pm 1$ and $\sigma = \pm 1$ are valley and spin indices which in our considerations always appear as a product $\sigma\xi$, so that a single composite index $\nu = \sigma\xi = \pm 1$ could be introduced. This leads to a double degeneracy of all considered dispersion relations and a transformation $\sum_{\xi,\sigma=\pm 1} \implies 2 \cdot \sum_{\nu=\pm 1}$, which we will use throughout this work.

For a number of cases of 2D structures, Eq.(4) could be immediately evaluated using the following property of a delta function

$$\delta(f(x)) = \sum_i \frac{\delta(x - x_i)}{|df(x)/dx|_{x=x_i}}, \quad (\text{A2})$$

where x_i are the roots of $f(x)$, formally given as $f(x) = \mathbb{E} - \varepsilon_\nu^\gamma(k)$ for various energy dispersions $\varepsilon_\nu^\gamma(k)$. In the case of silicene and germanene, the result is straightforward with

$$\rho_d(\mathbb{E}) = \frac{1}{\pi} \sum_{\gamma=\pm 1} \frac{\gamma \mathbb{E}}{\hbar^2 v_F^2} \sum_{i=<,>} \Theta \left[\frac{\mathbb{E}}{\gamma} - \Delta_i \right], \quad (\text{A3})$$

i.e., the DOS for Dirac gapped systems is linear similar to graphene. However, it is finite only above the energy gaps. This result also covers the case for gapped graphene if the two gaps are equal $\Delta_{<} = \Delta_{>} = \Delta_0$. Furthermore, we arrive at well-known V-shaped $\sim \mathbb{E}$ DOS for pristine gapless graphene if $\Delta_{<,>} \rightarrow 0$.

Molybdenum disulfide

In our work, we discuss several effective models of different complexity and accuracy, describing the energy dispersion $\varepsilon_\gamma^\nu(k)$ for MoS_2 . First, we consider a spin- and valley- resolved gapped graphene model given by Eq. (13), in which we leave out all the mass $\sim \alpha$ and $\sim \beta$ terms. It gives quite accurate results for the energy eigenstates next to the corners of Brillouin zone, as shown in Fig. 1. However, it is straightforward to see that the corresponding DOS obtained as

$$\rho_d(\mathbb{E}) = \frac{1}{\pi (t_0 a_0)^2} \sum_{\gamma=\pm 1} \frac{1}{\gamma} \sum_{\nu=\pm 1} \left(\mathbb{E} - \frac{\nu \lambda_0}{2} \right) \Theta \left[\gamma \left(\mathbb{E} - \frac{\nu \lambda_0}{2} \right) - \frac{1}{2} (\Delta - \nu \lambda_0) \right], \quad (\text{A4})$$

is V-shaped and does not match the numerical results even near the band edges. Once we get into the "allowed" energy ranges outside the band gap $\varepsilon_{\gamma=1}^{\nu=-1,1}(k=0) = \Delta/2$ for electrons, $\varepsilon_{\gamma=-1}^{\nu=-1}(k=0) = -\Delta/2 + \lambda_0$ and $\varepsilon_{\gamma=-1}^{\nu=1}(k=0) = -\Delta/2 - \lambda_0$ for the holes, the DOS experiences three different giant discontinuities due to each new contributing energy subband. These giant leaps could be calculated using the parabolic subbands approximation, obtained for $k \ll k_F$

$$\varepsilon_\gamma^\nu(k) = \frac{1}{2} [\nu \lambda_0 (1 - \gamma) + \gamma \Delta] + \left[\frac{\hbar^2}{4m_e} (\alpha + \gamma \beta) + \frac{\gamma (t_0 a_0)^2}{\Delta - \nu \lambda_0} \right] k^2. \quad (\text{A5})$$

This result leads to the DOS given by ⁸¹

$$\rho_d(\mathbb{E}) = \frac{1}{2\pi \hbar^2} \sum_{\gamma, \nu=\pm 1} \left| \frac{\alpha + \gamma \beta}{4m_e} + \frac{\gamma (t_0 a_0)^2}{\hbar^2 (\Delta - \nu \lambda_0)} \right|^{-1} \Theta \left[\gamma \left(\mathbb{E} - \frac{\nu \lambda_0}{2} \right) - \frac{1}{2} (\Delta - \nu \lambda_0) \right]. \quad (\text{A6})$$

The two terms in Eq. (A6) are of the same order of magnitude, consequently, each of them must be retained in our calculation. Physically it means that due to large gap Δ the curvature of each subband at $k=0$ is so small that even the $\simeq \alpha/(4m_e)$ correction is significant. It basically discards the DOS obtained for the gapped graphene model, even at $k \rightarrow 0$. The fact that the mass and even higher order terms must be taken into account for the plasmon calculation was mentioned in Ref. [38].

The principal model which yields quite reliable results for the DOS is derived by neglecting only non-essential $\mathcal{O}(k^4)$ terms with

$$\varepsilon_\gamma^\nu(k) \simeq \frac{1}{2} \nu \lambda_0 + \frac{\hbar^2 \alpha}{4m_e} k^2 + \frac{\gamma}{2} \sqrt{(\Delta - \nu \lambda_0)^2 + \left[(2t_0 a_0)^2 + (\Delta - \nu \lambda_0) \frac{\hbar^2 \beta}{m_e} \right] k^2}. \quad (\text{A7})$$

Here, all $\sim k^2$ terms are retained and the final expression for the DOS appears to be quite complicated. We use a general equation from our previous work ⁸¹ to come up with a linear approximation which, according to the most precise and generalized numerical results, ^{38,81} is valid for all experimentally allowable electron and hole doping densities. For the dispersions Eq. (A7), we use Eq. (A1) to obtain

$$\rho_d(\mathbb{E}) = \frac{1}{2\pi} \sum_j \sum_{\gamma, \nu=\pm 1} \left| \tilde{\alpha} + \frac{\gamma \tilde{A}_\nu(\Delta \pm \lambda_0, \beta | a_0 t_0)}{2 \left\{ \mathbb{E} - \tilde{\varepsilon}_\nu - \tilde{\alpha} \xi_\nu^{(j)}(\mathbb{E}) \right\}} \right|^{-1} \Theta \left[\gamma \left(\mathbb{E} - \frac{\mu \lambda_0}{2} \right) - \frac{1}{2} (\Delta - \nu \lambda_0) \right], \quad (\text{A8})$$

where $\tilde{\epsilon}_\nu = \nu\lambda_0/2$, $\tilde{\Delta}_\nu = (\Delta - \nu\lambda_0)/2$, $\tilde{A}_\nu(\Delta \pm \lambda_0, \beta | a_0 t_0) = (\Delta - \nu\lambda_0)\hbar^2\beta/(4m_e) + (t_0 a_0)^2$, and $\tilde{\alpha} = \hbar^2\alpha/(4m_e)$. $\xi_\nu^{(j)}(\mathbb{E})$ are the roots of

$$f(\mathbb{E}, \xi) = \mathbb{E} - \tilde{\epsilon}_\nu - \alpha\xi - \gamma\sqrt{\tilde{A}_\nu\xi + \tilde{\Delta}_\nu^2} = 0. \quad (\text{A9})$$

This equation could be solved by expressing it in quadratic form. However, one must bear in mind that if both parts of Eq. (A9) are squared, there might be additional non-physical solutions which must be disregarded. If this equation is written as $(\alpha\xi)^2 + B\xi + C = 0$, where $B = \tilde{A}_\nu + 2\alpha$ and $C = (\mathbb{E} - \tilde{\epsilon}_\nu)^2 - \tilde{\Delta}_\nu^2$, the only appropriate solution is $\xi^{(1)}(\mathbb{E}) = 1/(2\alpha)^2 (B + \sqrt{B^2 - 4\alpha^2 C})$. The other solution corresponds to the $\mathbb{E} - \tilde{\epsilon}_\nu - \alpha\xi = -\gamma\sqrt{\tilde{A}_\nu\xi + \tilde{\Delta}_\nu^2}$ and is obviously incorrect for $\alpha \rightarrow 0$. We also note that the electron/hole index γ is no longer present in this equation, so that the two \pm solutions are not associated with electron or hole states.

In order to illustrate the physics behind selecting the only appropriate solution, let us consider a simple example of gapless graphene with $\varepsilon_\gamma(k) = \hbar v_F k$ with additional small, not depending on γ , the mass term $\sim \alpha k^2$, $\alpha \ll \hbar v_F/k_F$. The actual dispersion relation is now $\varepsilon^\gamma(k) = \gamma\hbar v_F|k| + \alpha k^2$, and the DOS is calculated as

$$\rho_d(\mathbb{E}) = \frac{2}{\pi} \sum_{\gamma=\pm 1} \sum_j \frac{k^{(j)}}{|\gamma\hbar v_F + 2\alpha k^{(j)}|}. \quad (\text{A10})$$

The roots $k^{(j)}$ are the solutions of $\gamma\hbar v_F|k| + \alpha k^2 = 0$. Even though such a quadratic equation generally has two inequivalent solutions, only one of them $\pm k^{(1)} \simeq \mathbb{E}/(\gamma\hbar v_F) - \alpha\mathbb{E}^2/(\hbar^3 v_F^3)$ satisfies the $|k|$ -type equation. Consequently, we obtain the following expression

$$\rho_d(\mathbb{E}) \simeq \frac{2}{\pi} \sum_{\gamma=\pm 1} \frac{\mathbb{E}}{\gamma(\hbar v_F)^2} - \frac{\alpha(2+\gamma)\mathbb{E}^2}{(\hbar v_F)^4} \quad (\text{A11})$$

becoming equivalent to graphene DOS $\rho_d(\mathbb{E}) = 2/\pi \mathbb{E}/[\gamma(\hbar v_F)^2]$ for $\alpha \rightarrow 0$. For the holes with $\gamma = -1$, however, the linear and quadratic mass terms are competing, so that for $k \gg k_F$, another solution is present. However such wave vectors are beyond the Dirac cone model, and therefore, it is not physically acceptable. The obtained correction to the DOS is a small decrease, as it is expected to be for an energetically elevated location of the subband. However, in our model for MoS_2 , the mass terms $\sim \alpha$ and $\sim \beta$ are not small and represent a finite correction to the DOS. The small parameter which we used in our series expansions is the energy $\delta\epsilon$ above each band gap.

Now, we return to Eq. (A9) and present its solution as

$$\xi^{(1)} = \frac{1}{2\tilde{\alpha}^2} \left\{ \tilde{A}_\nu + 2\tilde{\alpha} \left(\mathbb{E} - \tilde{\epsilon}_\nu^{(0)} \right) - \left[\tilde{A}_\nu^2 + 4\tilde{\alpha}^2\tilde{\Delta}_\nu^2 + 4\tilde{\alpha}\tilde{A}_\nu \left(\mathbb{E} - \tilde{\epsilon}_\nu^{(0)} \right) \right]^{1/2} \right\}. \quad (\text{A12})$$

This solution is exact in the sense that no approximations have been made so far except for the $\sim k^2$ dispersions (A7). Substituted into Eq. (A8), it gives the DOS for an arbitrary energy, for both electrons and holes.

As the next step, we substitute this result for $\xi^{(1)}$ into Eq. (A8). We are interested in obtaining a linear approximation of the DOS next to each subband edge. Let us first consider electrons with $\varepsilon_1'(k) = \Delta/2 + \delta\epsilon$, $\delta\epsilon \ll \mathbb{E}$. In this case,

$$\xi_\nu^{(1)} \simeq \frac{4m_e}{\alpha\hbar^2} \left\{ 1 - \frac{(a_0 t_0)^2 + \hbar^2\beta/(4m_e) (\Delta - \nu\lambda_0)}{(a_0 t_0)^2 + \hbar^2/(4m_e) [(\alpha + \beta) (\Delta - \nu\lambda_0)]} \right\} \delta\epsilon, \quad (\text{A13})$$

and the DOS is now approximately given by

$$\rho_d(\mathbb{E}) = \frac{1}{2\pi} \sum_{\nu=\pm 1} \frac{\Delta - \nu\lambda_0}{(a_0 t_0)^2 + \hbar^2/(4m_e) (\alpha + \beta) (\Delta - \nu\lambda_0)} + \frac{2\delta\epsilon [(a_0 t_0)^2 + \hbar^2\beta/(4m_e) (\Delta - \nu\lambda_0)]^2}{\{(a_0 t_0)^2 + \hbar^2/(4m_e) [(\alpha + \beta) (\Delta - \nu\lambda_0)]\}^3}. \quad (\text{A14})$$

The actual numerical results are determined from

$$\begin{aligned}\rho_d(\mathbb{E}) &= c_0^{(3)} + c_1^{(3)} \left(\mathbb{E} - \frac{\Delta}{2} \right), \\ c_0^{(3)} &= 0.180 \frac{1}{t_0 a_0^2} = 11.74 \frac{E_F^{(0)}}{(\hbar v_F)^2}, \\ c_1^{(3)} &= 0.268 \frac{1}{(t_0 a_0)^2} = 1.218 \frac{1}{(\hbar v_F)^2}.\end{aligned}\tag{A15}$$

In the valence band, we consider two separate hole subbands with $\nu = \pm 1$. If $\gamma = -1$, $\nu = 1$ and $\mathbb{E} \leq -\Delta/2 + \lambda_0$, the DOS is $\rho_d(\mathbb{E}) = c_0^{(2)} + c_1^{(2)} \left[\mathbb{E} - \left(\frac{\Delta}{2} - \lambda_0 \right) \right]$, and the expansion coefficients are

$$\begin{aligned}c_0^{(2)} &= \frac{1}{2\pi} \frac{\Delta - \lambda_0}{(a_0 t_0)^2 + (\beta - \alpha)(\Delta - \lambda_0)}, \\ c_1^{(2)} &= \frac{1}{\pi} \frac{\delta\epsilon \left[(a_0 t_0)^2 + \hbar^2 \beta / (4m_e) (\Delta - \lambda_0) \right]^2}{\left\{ (a_0 t_0)^2 + \hbar^2 / (4m_e) [(\beta - \alpha) (\Delta - \lambda_0)] \right\}^3} < 0,\end{aligned}\tag{A16}$$

or

$$\begin{aligned}c_0^{(2)} &= 0.105 \frac{1}{t_0 a_0^2} = 6.847 \frac{E_F^{(0)}}{(\hbar v_F)^2}, \\ c_1^{(2)} &= -0.232 \frac{1}{(t_0 a_0)^2} = -1.051 \frac{1}{(\hbar v_F)^2}.\end{aligned}\tag{A17}$$

Finally, for the lower hole subband with $\mathbb{E} \lesssim -\Delta/2 - \lambda_0$, we obtain

$$\begin{aligned}\rho_d(\mathbb{E}) &= c_0^{(2)} + c_1^{(2)} \left[\mathbb{E} - \left(\frac{\Delta}{2} + \lambda_0 \right) \right], \\ c_0^{(1)} &= \frac{1}{2\pi} \sum_{\nu=\pm 1} \frac{\Delta - \nu \lambda_0}{(a_0 t_0)^2 + (\beta - \alpha)(\Delta - \nu \lambda_0)}, \\ c_1^{(1)} &= \frac{1}{\pi} \sum_{\nu=\pm 1} \frac{\delta\epsilon \left[(a_0 t_0)^2 + \hbar^2 \beta / (4m_e) (\Delta - \nu \lambda_0) \right]^2}{\left\{ (a_0 t_0)^2 + \hbar^2 / (4m_e) [(\beta - \alpha) (\Delta - \nu \lambda_0)] \right\}^3} < 0,\end{aligned}\tag{A18}$$

and

$$\begin{aligned}c_0^{(1)} &= 0.233 \frac{1}{t_0 a_0^2} = 15.17 \frac{E_F^{(0)}}{(\hbar v_F)^2}, \\ c_1^{(1)} &= -0.458 \frac{1}{(t_0 a_0)^2} = 2.077 \frac{1}{(\hbar v_F)^2}.\end{aligned}\tag{A19}$$

It is straightforward to obtain our previous results for the gapped graphene model (A4) DOS if $\alpha = \beta \rightarrow 0$. We also note that the slope of the DOS in the conduction band is negative, as it should be according to Fig. 1 (d), and the summation over the ν index is present in all cases except the upper hole subband in Eqs. (A16).

Our results (A15) - (A19) (here, we move from the conduction electrons to the valence band, i.e., from the right to left) represent a fairly good match with the previously obtained numerical values, specified in Sec. II and later used for all our finite temperature calculations. The coefficients $c_0^{(i)}$, $i = 1, 2, 3$ are equal to the giant discontinuities of the DOS $\delta\rho_d(\mathbb{E})$ at each subband edge or $k = 0$, except $c_0^{(1)} \simeq \delta\rho_d^{(2)}(-\Delta/2 + \lambda_0) + \delta\rho_d^{(1)}(-\Delta/2 - \lambda_0)$, and, therefore, are accurate. The linear coefficients $c_1^{(i)}$, in fair agreement, are 20 - 25% larger compared with the numerical results since all the $\sim k^4$ terms of our energy dispersions are neglected. Inclusion of these terms leads to the higher energies

for chosen wave vector and a decrease of the DOS. This discrepancy is increased for higher energies, which is well seen for $c_1^{(1)}$ for holes with $\mathbb{E} < -\Delta/2 - \lambda_0$. However, the subbands for such energy ranges do not receive any substantial doping unless the temperature becomes very high. For most considered situations, we are limited for $\delta\epsilon \approx \lambda_0$ within the band edges. In such a small range, $c_1^{(i)} \delta\epsilon \ll c_0^{(i)}$, so that the actual DOS values remain almost unaffected and our model yields accurate results.

Appendix B: Chemical potential $\mu = \mu(T)$ at a finite temperature

We now derive a set of algebraic equations for the finite-temperature chemical potential $\mu(T)$. At zero temperature, it is equal to the Fermi energy $E_F = \mu(T)|_{T=0}$. Our derivation is based on the total carrier density conservation, which includes both electrons and holes, for zero and any finite temperatures ⁷³

$$n = n^{(e)} + (-1)n^{(h)} = \int_0^\infty d\mathbb{E} \rho_d(\mathbb{E}) f_{\gamma=1}(\mathbb{E}, T) - \int_{-\infty}^0 d\mathbb{E} \rho_d(\mathbb{E}) \{1 - f_{\gamma=1}(\mathbb{E}, T)\}. \quad (\text{B1})$$

The electron and hole occupation probabilities are complimentary and for electron doping at $T = 0$ the hole states term has no effect on Eq. (B1) (for details see Ref. [100]).

We begin with the relatively simple case for silicene with dispersions (3). The DOS $\rho_d(\mathbb{E})$ for which buckled honeycomb lattices is given by Eq. (4). The expression for the Fermi energy E_F for fixed electron doping density n at zero temperature depends on whether either one or both electron subbands are doped. The former case occurs for doping densities

$$n \leq n_c = \frac{1}{2\pi} \frac{\Delta_{>}^2 - \Delta_{<}^2}{\hbar^2 v_F^2} = \frac{2}{\pi \hbar^2 v_F^2} \Delta_{SO} \Delta_z, \quad (\text{B2})$$

and the Fermi energy is obtained from

$$n = \frac{1}{2\pi} \frac{E_F^2 - \Delta_{<}^2}{\hbar^2 v_F^2}. \quad (\text{B3})$$

Alternatively, if the doping density is sufficient to populate both subbands, E_F is determined by

$$n = \frac{1}{\pi} \frac{1}{\hbar^2 v_F^2} \left[E_F^2 - \frac{1}{2} (\Delta_{<}^2 + \Delta_{>}^2) \right]. \quad (\text{B4})$$

Once the temperature is set finite, Eq. (B1) leads us to $n = \mathcal{I}^{(e)}(\Delta_i, T) - \mathcal{I}^{(h)}(\Delta_i, T)$, with the two terms corresponding to electron and hole components of the total carrier density. These integrals are presented as

$$\mathcal{I}^{(e)}(\Delta_i, T) = \int_{\Delta_{<}}^\infty d\mathbb{E} \mathcal{A}(\mathbb{E}, T) + \int_{\Delta_{>}}^\infty d\mathbb{E} \mathcal{A}(\mathbb{E}, T), \quad (\text{B5})$$

where

$$\mathcal{A}(\mathbb{E}, T) = \frac{1}{\pi} \frac{\mathbb{E}}{\hbar^2 v_F^2} \left\{ 1 + \exp \left[\frac{\mathbb{E} - \mu(T)}{k_B T} \right] \right\}^{-1}. \quad (\text{B6})$$

Each of these integrals could be easily evaluated. Using a variable substitution $\xi = (\mathbb{E} - \Delta_{<})/k_B T$, we obtain

$$\frac{1}{\pi} \frac{1}{(\hbar v_F)^2} \int_{\Delta_{<}}^\infty d\mathbb{E} \mathbb{E} \left\{ 1 + \exp \left[\frac{\mathbb{E} - \mu(T)}{k_B T} \right] \right\}^{-1} = \frac{k_B T}{\pi (\hbar v_F)^2} \int_0^\infty d\xi (\Delta_{<} + \xi k_B T) \left\{ 1 + \exp \left[\xi - \frac{\mu(T) - \Delta_{<}}{k_B T} \right] \right\}^{-1} \quad (\text{B7})$$

With the help of the following notation

$$\mathcal{R}^{(p)}(T, X) = \int_0^\infty d\xi \xi^p / \{1 + \exp[\xi - X/(k_B T)]\}, \quad (\text{B8})$$

we obtain the final result of the integration as

$$\frac{k_B T \Delta_{<}}{\pi (\hbar v_F)^2} \mathcal{R}^{(0)}[T, \mu(T) - \Delta_{<}] + \frac{1}{\pi} \left(\frac{k_B T}{\hbar v_F} \right)^2 \mathcal{R}^{(1)}[T, \mu(T) - \Delta_{<}]. \quad (\text{B9})$$

For $p = 0$ and 1 , corresponding to the 2DEG and gapless graphene, Eq. (B8) leads to ^{101,102}

$$\begin{aligned} \mathcal{R}^{(0)}(T, X) &= \ln \left\{ 1 + \exp \left[\frac{X}{k_B T} \right] \right\}, \\ \mathcal{R}^{(1)}(T, X) &= -\text{Li}_2 \left\{ -\exp \left[\frac{X}{k_B T} \right] \right\}, \end{aligned} \quad (\text{B10})$$

where $\text{Li}_2(z)$ is the *second-order polylogarithm function* or *dilogarithm* defined as

$$\begin{aligned} \text{Li}_p(z) &= \sum_{k=1}^{\infty} \frac{z^k}{k^p}, \\ \text{Li}_2(z) &= -\int_0^z \frac{\ln(1-t)}{t} dt. \end{aligned} \quad (\text{B11})$$

The second term of Eq.(B5), which only differs from the first one by its integration limits, is

$$\frac{2k_B T \Delta_{>}}{\pi (\hbar v_F)^2} \ln \left\{ 1 + \exp \left[\frac{\mu(T) - \Delta_{>}}{k_B T} \right] \right\} - \frac{1}{\pi} \left(\frac{k_B T}{\hbar v_F} \right)^2 \text{Li}_2 \left\{ -\exp \left[\frac{\mu(T) - \Delta_{>}}{k_B T} \right] \right\}. \quad (\text{B12})$$

The remaining term $\mathcal{I}^{(h)}(\Delta_i, T)$, $i = \{<, >\}$, which describes the contribution from the holes, is also easily obtained

$$\begin{aligned} \mathcal{I}^{(h)}(\Delta_i, T) &= \mathcal{I}_1^{(h)}(\Delta_i, T) + \mathcal{I}_2^{(h)}(\Delta_i, T) \quad \text{where,} \\ \mathcal{I}_1^{(h)}(\Delta_i, T) &= \frac{1}{\pi} \frac{k_B T}{(\hbar v_F)^2} \sum_{i=\{<, >\}} \Delta_i \mathcal{R}^{(0)} \{T, -[\mu(T) + \Delta_i]\} \quad \text{and} \\ \mathcal{I}_2^{(h)}(\Delta_i, T) &= \frac{1}{\pi} \left(\frac{k_B T}{\hbar v_F} \right)^2 \sum_{i=\{<, >\}} \mathcal{R}^{(1)} \{T, -[\mu(T) + \Delta_i]\}. \end{aligned} \quad (\text{B13})$$

Now, the total carrier density from Eq. (B1) could be written as

$$n = \left(\frac{k_B T}{\hbar v_F} \right)^2 \sum_{\gamma=\pm 1} \frac{\gamma}{\pi} \sum_{i=\{<, >\}} \mathcal{R}^{(1)} [T, \gamma\mu(T) - \Delta_i] + \frac{\Delta_i}{k_B T} \mathcal{R}^{(0)} [T, \gamma\mu(T) - \Delta_i] \quad (\text{B14})$$

or, explicitly expressing the polylogarithm functions, we write

$$n \left(\frac{\hbar v_F}{k_B T} \right)^2 = \sum_{\gamma=\pm 1} \frac{\gamma}{\pi} \sum_{i=\{<, >\}} -\text{Li}_2 \left\{ -\exp \left[\frac{\gamma\mu(T) - \Delta_i}{k_B T} \right] \right\} + \frac{\Delta_i}{k_B T} \ln \left\{ 1 + \exp \left[\frac{\gamma\mu(T) - \Delta_i}{k_B T} \right] \right\}. \quad (\text{B15})$$

Using Eqs. (B3) or Eq. (B4) depending on whether only one or both subbands are filled at zero temperature, we obtain the equation which relates the finite-temperature chemical potential with its $T = 0$ value E_F . Energy band gap(s) obviously affects this result.

The $\mu(T)$ for gapped graphene with two fourfold degenerate energy subbands is obtained if we substitute $\Delta_{<} = \Delta_{>} = \Delta_0$ and $\sum_{i=<,>} \implies \times 2$. For gapless graphene, $\Delta_0 = 0$ and $\pi n = [E_F/(\hbar v_F)]^2$, so that we write

$$\frac{1}{2(k_B T)^2} E_F^2 = \sum_{\gamma=\pm 1} \gamma \mathcal{R}^{(1)}[T, \gamma\mu(T)] = - \sum_{\gamma=\pm 1} \gamma \text{Li}_2 \left\{ -\exp \left[\frac{\gamma\mu(T)}{k_B T} \right] \right\}. \quad (\text{B16})$$

If the temperature is kept low with $k_B T \ll E_F$, this result is simplified as ⁷³

$$\mathcal{R}^1(x) \simeq \left(\frac{x^2}{2} + \frac{\pi^2}{6} \right) \Theta(x) + x \ln(1 + e^{-|x|}), \quad (\text{B17})$$

Finalizing our derivations for silicene, we briefly address the case of hole doping with $E_F < 0$. The left part of Eq. (B1) is now modified as

$$-n^{(h)} = -\frac{2}{\pi} \frac{1}{(\hbar v_F)^2} \sum_{i=<,>} \int_{-\infty}^{-\Delta_i} d\mathbb{E} |\mathbb{E}| \Theta(-\mathbb{E} + E_F). \quad (\text{B18})$$

In analogy with electron doping, the Fermi energy depends on whether only the $\Delta_{<}$ -subband (which is now the higher one) or they are both doped. The equations determining the Fermi energy for given hole doping density n are exactly similar to Eqs. (B3) and (B4), which confirms complete symmetry between the electron and hole states in silicene. The right part of Eq. (B1) remains unchanged except the chemical potential is negative $\mu < 0$ for any finite temperature.

$\mu(T)$ for transition metal dichalcogenides

In contrast to the previously considered buckled honeycomb lattices and graphene, the electron/hole symmetry in TMDC's (such as MoS_2) is clearly broken. Even in the simplest gapped graphene model given by Eq. (13), the two hole subbands are not degenerate and separated by λ_0 at $k = 0$. For all reasonable doping densities $n < 10^{17} m^{-2}$, the Fermi energy is such that the lower $\varepsilon_{\nu=1}^{\gamma=-1}(k=0) = -\Delta/2 - \lambda_0$ subband *could not be populated* at zero temperature. This could be verified by rewriting Eq. (B2) as

$$n_c = \frac{2}{\pi} \frac{\lambda_0 \Delta}{(t_0 a_0)^2} = 1.0 \cdot 10^{18} m^{-2}. \quad (\text{B19})$$

From here on, we are going to use a piecewise-linear model for the DOS with the empirical coefficients, provided in Sec. II. Our analytical model for the DOS, develop in the preceding Appendix in Eqs. (A15) - (A19) could also be employed here without losing much of precision. Let's us first consider electron doping with density $n_{(0)}^e$ at zero temperature. The corresponding Fermi energy is determined by

$$n_{(0)}^e = c_1^{(3)}/2 (E_F^2 - \Delta^2/4) + c_0^{(3)} (E_F - \Delta/2), \quad (\text{B20})$$

or

$$E_F^e = \frac{1}{c_1^{(3)}} \left\{ -c_0^{(3)} + \left[\left(c_0^{(3)} + c_1^{(3)} \frac{\Delta}{2} \right)^2 + 2n_{(0)}^e c_1^{(3)} \right]^{1/2} \right\}. \quad (\text{B21})$$

For hole doping the result is quite similar, except $c_1^{(2)} < 0$ and the upper valence band gap is $-\Delta/2 + \lambda_0$:

$$E_F^{(h)} = \frac{1}{c_1^{(2)}} \left\{ -c_0^{(2)} + \left\{ -2c_1^{(2)} n_{(0)}^h + \left[c_0^{(2)} - c_1^{(2)} \left(\frac{\Delta}{2} - \lambda_0 \right) \right]^2 \right\}^{1/2} \right\}. \quad (\text{B22})$$

Using this expression, we can further improve the result in Eq. (B19) for the critical hole doping density n_c needed to reach the lower subband at zero temperature. The required Fermi energy is $E_F^{(h)} \leq -\Delta/2 - \lambda_0$, so that the corresponding hole density is $n_c^h = -\lambda_0 \Delta c_1^{(2)} + 2c_0^{(2)} \lambda_0 = 3.3 \cdot 10^{17} m^{-2}$.

This critical density value is still far above the experimentally realizable values $\simeq 1.0 \cdot 10^{17} m^{-2}$, and for all our calculations, the lower hole subband *is never populated* at $T = 0$.

Finally, we address the finite-temperature chemical potential for MoS_2 . Once again, we start with the carrier density conservation equation (B1).

The electron component is easily evaluated as

$$k_B T \left(c_0^{(3)} + \frac{\Delta}{2} \right) \mathcal{R}^{(0)} \left[T, \mu(T) - \frac{\Delta}{2} \right] + c_1^{(3)} (k_B T)^2 \mathcal{R}^{(1)} \left[T, \mu(T) - \frac{\Delta}{2} \right]. \quad (\text{B23})$$

The hole state integrals are written in the following form

$$\begin{aligned} \int_{-\infty}^0 d\mathbb{E} \rho_d(|\mathbb{E}|) \{1 - f_1(\mathbb{E}, \mathbb{T})\} &= \int_{-\infty}^{-\Delta/2+\lambda_0} d\mathbb{E} \left[-c_1^{(2)} \mathbb{E} + c_0^{(2)} \right] \left\{ 1 + \exp \left[\frac{\mu(T) - \mathbb{E}}{k_B T} \right] \right\}^{-1} + \\ &+ \int_{-\infty}^{-\Delta/2-\lambda_0} d\mathbb{E} \left[-\delta c_1^{(1)} \mathbb{E} + \delta c_0^{(1)} \right] \left\{ 1 + \exp \left[\frac{\mu(T) - \mathbb{E}}{k_B T} \right] \right\}^{-1}, \end{aligned} \quad (\text{B24})$$

where $\delta c_1^{(i)} = c_1^{(i)} - c_2^{(i)}$, $i = 1, 2$. They are evaluated as

$$\begin{aligned} \mathcal{I}^{(h)}(\Delta, \lambda_0 | T) &= \sum_{j=1}^4 \mathcal{I}_j^{(h)} \quad \text{where,} \\ \mathcal{I}_1^{(h)}(\Delta, \lambda_0 | T) &= k_B T \left(\frac{\Delta}{2} - \lambda_0 + c_2^{(0)} \right) \mathcal{R}^{(0)} \left\{ T, - \left[\mu(T) + \frac{\Delta}{2} - \lambda_0 \right] \right\}, \\ \mathcal{I}_2^{(h)}(\Delta, \lambda_0 | T) &= c_2^{(1)} (k_B T)^2 \mathcal{R}^{(1)} \left\{ T, - \left[\mu(T) + \frac{\Delta}{2} - \lambda_0 \right] \right\}, \\ \mathcal{I}_3^{(h)}(\Delta, \lambda_0 | T) &= k_B T \left(\frac{\Delta}{2} + \lambda_0 + \delta c_1^{(0)} \right) \mathcal{R}^{(0)} \left\{ T, - \left[\mu(T) + \frac{\Delta}{2} + \lambda_0 \right] \right\}, \\ \mathcal{I}_2^{(h)}(\Delta, \lambda_0 | T) &= \delta c_1^{(1)} (k_B T)^2 \mathcal{R}^{(1)} \left\{ T, - \left[\mu(T) + \frac{\Delta}{2} + \lambda_0 \right] \right\}. \end{aligned} \quad (\text{B25})$$

Combined with the electron terms (B23), these hole integrals (B26) form the right side of the carrier density conservation (B1). Its left side, corresponding to zero temperature, is given by Eq. (B20) for electron doping and by

$$n_{(0)}^e = \left(\frac{\Delta}{2} + E_F - \lambda_0 \right) \left\{ c_2^{(0)} + \frac{c_2^{(1)}}{2} \left[\frac{\Delta}{2} - (E_F + \lambda_0) \right] \right\}, \quad (\text{B26})$$

for hole doping. The symmetry between the electron and hole states is no longer present, which strongly affects the finite-temperature behavior of the chemical potential in TMDC's.

* Electronic address: aiurov@unm.edu

- ¹ T. Ando, A. B. Fowler, and F. Stern, *Reviews of Modern Physics* **54**, 437 (1982).
- ² F. Stern, *Phys. Rev. Lett.* **18**, 546 (1967).
- ³ K. Novoselov, A. K. Geim, S. Morozov, D. Jiang, M. Katsnelson, I. Grigorieva, S. Dubonos, and A. Firsov, *nature* **438**, 197 (2005).
- ⁴ A. K. Geim and K. S. Novoselov, *Nature materials* **6**, 183 (2007).
- ⁵ A. C. Neto, F. Guinea, N. Peres, K. S. Novoselov, and A. K. Geim, *Reviews of modern physics* **81**, 109 (2009).
- ⁶ A. C. Neto, F. Guinea, N. M. Peres, K. S. Novoselov, and A. K. Geim, *Reviews of modern physics* **81**, 109 (2009).
- ⁷ P. Avouris, *Nano letters* **10**, 4285 (2010).
- ⁸ H.-R. Chang, J. Zhou, H. Zhang, and Y. Yao, *Phys. Rev. B* **89**, 201411 (2014).
- ⁹ G. Giovannetti, P. A. Khomyakov, G. Brocks, P. J. Kelly, and J. van den Brink, *Physical Review B* **76**, 073103 (2007).
- ¹⁰ N. Kharche and S. K. Nayak, *Nano letters* **11**, 5274 (2011).
- ¹¹ Z. H. Ni, T. Yu, Y. H. Lu, Y. Y. Wang, Y. P. Feng, and Z. X. Shen, *ACS nano* **2**, 2301 (2008).
- ¹² O. Kibis, *Physical Review B* **81**, 165433 (2010).
- ¹³ X. Li, X. Wang, L. Zhang, S. Lee, and H. Dai, *science* **319**, 1229 (2008).
- ¹⁴ Y.-W. Son, M. L. Cohen, and S. G. Louie, *Physical review letters* **97**, 216803 (2006).
- ¹⁵ M. Y. Han, B. Özyilmaz, Y. Zhang, and P. Kim, *Physical review letters* **98**, 206805 (2007).
- ¹⁶ M. Ezawa, *New Journal of Physics* **14**, 033003 (2012).
- ¹⁷ C. J. Tabert and E. J. Nicol, *Phys. Rev. B* **89**, 195410 (2014).
- ¹⁸ B. Lalmi, H. Oughaddou, H. Enriquez, A. Kara, S. Vizzini, B. Ealet, and B. Aufray, *Applied Physics Letters* **97**, 223109 (2010).
- ¹⁹ C. L. Kane and E. J. Mele, *Phys. Rev. Lett.* **95**, 226801 (2005).
- ²⁰ M. Ezawa, *Phys. Rev. Lett.* **109**, 055502 (2012).
- ²¹ N. D. Drummond, V. Zólyomi, and V. I. Fal'ko, *Phys. Rev. B* **85**, 075423 (2012).
- ²² B. Aufray, A. Kara, S. Vizzini, H. Oughaddou, C. Leandri, B. Ealet, and G. Le Lay, *Applied Physics Letters* **96**, 183102 (2010).
- ²³ P. De Padova, C. Quaresima, C. Ottaviani, P. M. Sheverdyaeva, P. Moras, C. Carbone, D. Topwal, B. Olivieri, A. Kara, H. Oughaddou, et al., *Applied Physics Letters* **96**, 261905 (2010).
- ²⁴ L. Zhang, P. Bampoulis, A. van Houselt, and H. Zandvliet, *Applied Physics Letters* **107**, 111605 (2015).
- ²⁵ A. Acun, L. Zhang, P. Bampoulis, M. Farmanbar, A. van Houselt, A. Rudenko, M. Lingenfelder, G. Brocks, B. Poelsema, M. Katsnelson, et al., *Journal of Physics: Condensed Matter* **27**, 443002 (2015).
- ²⁶ L. Li, S.-z. Lu, J. Pan, Z. Qin, Y.-q. Wang, Y. Wang, G.-y. Cao, S. Du, and H.-J. Gao, *Advanced Materials* **26**, 4820 (2014).
- ²⁷ M. Dávila, L. Xian, S. Cahangirov, A. Rubio, and G. Le Lay, *New Journal of Physics* **16**, 095002 (2014).
- ²⁸ P. Bampoulis, L. Zhang, A. Safaei, R. Van Gastel, B. Poelsema, and H. J. W. Zandvliet, *Journal of physics: Condensed matter* **26**, 442001 (2014).
- ²⁹ M. Derivaz, D. Dentel, R. Stephan, M.-C. Hanf, A. Mehdaoui, P. Sonnet, and C. Pirri, *Nano letters* **15**, 2510 (2015).
- ³⁰ F. dAcapito, S. Torrenco, E. Xenogiannopoulou, P. Tsipas, J. M. Velasco, D. Tsoutsou, and A. Dimoulas, *Journal of Physics: Condensed Matter* **28**, 045002 (2016).
- ³¹ R. Ganatra and Q. Zhang, *ACS nano* **8**, 4074 (2014).
- ³² H. Rostami, A. G. Moghaddam, and R. Asgari, *Physical Review B* **88**, 085440 (2013).
- ³³ K. Kośmider, J. W. González, and J. Fernández-Rossier, *Phys. Rev. B* **88**, 245436 (2013).
- ³⁴ D. Xiao, G.-B. Liu, W. Feng, X. Xu, and W. Yao, *Phys. Rev. Lett.* **108**, 196802 (2012).
- ³⁵ A. Kormányos, V. Zólyomi, N. D. Drummond, P. Rakytá, G. Burkard, and V. I. Fal'ko, *Phys. Rev. B* **88**, 045416 (2013).
- ³⁶ H. Rostami, R. Roldán, E. Cappelluti, R. Asgari, and F. Guinea, *Physical Review B* **92**, 195402 (2015).
- ³⁷ B. Radisavljevic, A. Radenovic, J. Brivio, i. V. Giacometti, and A. Kis, *Nature nanotechnology* **6**, 147 (2011).
- ³⁸ A. Scholz, T. Stauber, and J. Schliemann, *Phys. Rev. B* **88**, 035135 (2013).
- ³⁹ L. Wang, A. Kutana, and B. I. Yakobson, *Annalen der Physik* **526** (2014).
- ⁴⁰ O. Kibis, K. Dini, I. Iorsh, and I. Shelykh, *Physical Review B* **95**, 125401 (2017).
- ⁴¹ G. Giuliani and G. Vignale, *Quantum theory of the electron liquid* (Cambridge university press, 2005).
- ⁴² G. Gumbs and D. Huang, *Properties of Interacting Low-Dimensional Systems* (John Wiley & Sons, 2013).
- ⁴³ C. J. Tabert and E. J. Nicol, *Physical review letters* **110**, 197402 (2013).
- ⁴⁴ C. J. Tabert and E. J. Nicol, *Physical Review B* **87**, 235426 (2013).
- ⁴⁵ C. J. Tabert and E. J. Nicol, *Physical Review B* **88**, 085434 (2013).
- ⁴⁶ T. Ando, *Journal of the Physical Society of Japan* **75**, 074716 (2006).
- ⁴⁷ P. Pyatkovskiy, *Journal of Physics: Condensed Matter* **21**, 025506 (2008).
- ⁴⁸ S. D. Sarma, E. Hwang, and H. Min, *Physical Review B* **91**, 035201 (2015).
- ⁴⁹ O. Sobol, P. Pyatkovskiy, E. Gorbar, and V. Gusynin, *Physical Review B* **94**, 115409 (2016).
- ⁵⁰ B. Wunsch, T. Stauber, F. Sols, and F. Guinea, *New Journal of Physics* **8**, 318 (2006).
- ⁵¹ E. H. Hwang and S. Das Sarma, *Phys. Rev. B* **75**, 205418 (2007).
- ⁵² S. Das Sarma and Q. Li, *Phys. Rev. B* **87**, 235418 (2013).
- ⁵³ T. Stauber, J. Schliemann, and N. M. R. Peres, *Phys. Rev. B* **81**, 085409 (2010).
- ⁵⁴ A. Scholz, T. Stauber, and J. Schliemann, *Phys. Rev. B* **86**, 195424 (2012).
- ⁵⁵ T. Stauber, G. Gómez-Santos, and L. Brey, *arXiv preprint arXiv:1706.09403* (2017).
- ⁵⁶ S. Das Sarma and E. H. Hwang, *Phys. Rev. Lett.* **102**, 206412 (2009).

- ⁵⁷ H. Yan, T. Low, W. Zhu, Y. Wu, M. Freitag, X. Li, F. Guinea, P. Avouris, and F. Xia, *Nature Photonics* **7**, 394 (2013).
- ⁵⁸ J. Chen, M. Badioli, P. Alonso-González, S. Thongrattanasiri, F. Huth, J. Osmond, M. Spasenović, A. Centeno, A. Pesquera, P. Godignon, et al., *Nature* **487**, 77 (2012).
- ⁵⁹ X. Luo, T. Qiu, W. Lu, and Z. Ni, *Materials Science and Engineering: R: Reports* **74**, 351 (2013).
- ⁶⁰ A. Grigorenko, M. Polini, and K. Novoselov, *Nature photonics* **6**, 749 (2012).
- ⁶¹ J. H. Strait, P. Nene, W.-M. Chan, C. Manolatou, S. Tiwari, F. Rana, J. W. Kevek, and P. L. McEuen, *Physical Review B* **87**, 241410 (2013).
- ⁶² G. Gumbs, A. Iurov, D. Huang, and W. Pan, *Journal of Applied Physics* **118**, 054303 (2015).
- ⁶³ A. Politano and G. Chiarello, *Nanoscale* **6**, 10927 (2014).
- ⁶⁴ A. Politano, V. M. Silkin, I. A. Nechaev, M. S. Vitiello, L. Viti, Z. S. Aliev, M. B. Babanly, G. Chiarello, P. M. Echenique, and E. V. Chulkov, *Phys. Rev. Lett.* **115**, 216802 (2015).
- ⁶⁵ A. Politano, A. R. Marino, V. Formoso, D. Fariás, R. Miranda, and G. Chiarello, *Phys. Rev. B* **84**, 033401 (2011).
- ⁶⁶ A. Politano, A. R. Marino, and G. Chiarello, *Phys. Rev. B* **86**, 085420 (2012).
- ⁶⁷ A. Politano and G. Chiarello, *Applied Physics Letters* **102**, 201608 (2013).
- ⁶⁸ A. Politano and G. Chiarello, *2D Materials* **4**, 035003 (2017).
- ⁶⁹ A. Politano, I. Radović, D. Borka, Z. Mišković, H. Yu, D. Farias, and G. Chiarello, *Carbon* **114**, 70 (2017).
- ⁷⁰ S. Das Sarma and Q. Li, *Phys. Rev. B* **87**, 235418 (2013).
- ⁷¹ D. K. Patel, S. S. Ashraf, and A. C. Sharma, *physica status solidi (b)* **252**, 1817 (2015).
- ⁷² J. Wu, S. Chen, and M. Lin, *New Journal of Physics* **16**, 125002 (2014).
- ⁷³ E. H. Hwang and S. Das Sarma, *Phys. Rev. B* **79**, 165404 (2009).
- ⁷⁴ L. Meng, Y. Zhang, W. Yan, L. Feng, L. He, R.-F. Dou, and J.-C. Nie, *Applied Physics Letters* **100**, 091601 (2012).
- ⁷⁵ P. Plochocka, C. Faugeras, M. Orlita, M. L. Sadowski, G. Martinez, M. Potemski, M. O. Goerbig, J.-N. Fuchs, C. Berger, and W. A. De Heer, *Physical review letters* **100**, 087401 (2008).
- ⁷⁶ M. Pizarra, A. Sindona, P. Riccardi, V. Silkin, and J. Pitarke, *New Journal of Physics* **16**, 083003 (2014).
- ⁷⁷ V. Despoja, D. Novko, K. Dekanić, M. Šunjić, and L. Marušić, *Physical Review B* **87**, 075447 (2013).
- ⁷⁸ A. Iurov, G. Gumbs, and D. Huang, *Journal of Physics: Condensed Matter* **29**, 135602 (2017).
- ⁷⁹ C. Walhout, A. Acun, L. Zhang, M. Ezawa, and H. Zandvliet, *Journal of physics: Condensed matter* **28**, 284006 (2016).
- ⁸⁰ A. Iurov, G. Gumbs, D. Huang, and V. Silkin, *Physical Review B* **93**, 035404 (2016).
- ⁸¹ A. Iurov, G. Gumbs, D. Huang, and L. Zhemchuzhna, *Journal of Applied Physics* **121**, 084306 (2017).
- ⁸² D. Xiao, G.-B. Liu, W. Feng, X. Xu, and W. Yao, *Physical Review Letters* **108**, 196802 (2012).
- ⁸³ A. Scholz, T. Stauber, and J. Schliemann, *Physical Review B* **88**, 035135 (2013).
- ⁸⁴ P. F. Maldague, *Surface Science* **73**, 296 (1978).
- ⁸⁵ Y. Gogotsi and V. Presser, *Carbon nanomaterials* (CRC press, 2013).
- ⁸⁶ H. Raza, *Graphene nanoelectronics: metrology, synthesis, properties and applications* (Springer Science & Business Media, 2012).
- ⁸⁷ W. L. Barnes, A. Dereux, and T. W. Ebbesen, *Nature* **424**, 824 (2003).
- ⁸⁸ G. Gumbs, A. Iurov, and N. J. M. Horing, *Phys. Rev. B* **91**, 235416 (2015).
- ⁸⁹ M. Campisi, P. Hänggi, and P. Talkner, *Rev. Mod. Phys.* **83**, 771 (2011).
- ⁹⁰ G. Schaller, *Open quantum systems far from equilibrium*, vol. 881 (Springer, 2014).
- ⁹¹ N. J. Horing, A. Iurov, G. Gumbs, A. Politano, and G. Chiarello, in *Low-Dimensional and Nanostructured Materials and Devices* (Springer, 2016), pp. 205–237.
- ⁹² N. J. M. Horing, *Physical Review B* **80**, 193401 (2009).
- ⁹³ N. J. M. Horing, *Philosophical Transactions of the Royal Society of London A: Mathematical, Physical and Engineering Sciences* **368**, 5525 (2010).
- ⁹⁴ N. J. M. Horing, E. Kamen, and H.-L. Cui, *Physical Review B* **32**, 2184 (1985).
- ⁹⁵ G. Gumbs, A. Iurov, J.-Y. Wu, M. Lin, and P. Fekete, *Scientific reports* **6** (2016).
- ⁹⁶ C. Kramberger, R. Hambach, C. Giorgetti, M. H. Rummeli, M. Knupfer, J. Fink, B. Büchner, L. Reining, E. Einarsson, S. Maruyama, et al., *Phys. Rev. Lett.* **100**, 196803 (2008).
- ⁹⁷ E. d. A. e Silva, G. La Rocca, and F. Bassani, *Physical Review B* **55**, 16293 (1997).
- ⁹⁸ M. Burt, *Semiconductor science and technology* **3**, 739 (1988).
- ⁹⁹ M. Ezawa, *Applied Physics Letters* **102**, 172103 (2013).
- ¹⁰⁰ T. Izraeli, Final Project in the Computational Physics Course (2013).
- ¹⁰¹ E. W. Weisstein, *CRC concise encyclopedia of mathematics* (CRC press, 2002).
- ¹⁰² I. S. Gradshteyn and I. M. Ryzhik, *Table of integrals, series, and products* (Academic press, 2014).
- ¹⁰³ Expression $k_F = \sqrt{\pi n}$ holds true only for systems with a fourfold spin and valley degeneracy, such as graphene, i.e., $g = g_s g_v = 4$. The general equation for the Fermi momentum in a 2D material reads $(2\pi)^2 n = g \pi k_F$.
- ¹⁰⁴ Due to a large gap parameter $\Delta = 1.9 \text{ eV}$, the electronic states corresponding to large wave vectors are often involved and at $k \approx 5.0 k_F^{(0)}$ correction $\simeq \Delta \beta k^4$ is no longer negligible.